MAVEN Observations of Low Frequency Steepened Magnetosonic Waves and Associated Heating of the Martian Nightside Ionosphere

C. M. Fowler, K. G. Hanley, J. P. Mcfadden, C. C. Chaston, J. W. Bonnell, J. S. Halekas, J. R. Espley, G. A. Dibraccio, S. J. Schwartz, C. Mazelle, et al.

JGR Space Physics

RESEARCH ARTICLE
10.1029/2021JA029615

Key Points:

- Linear and steepened magnetosonic waves are observed in the near Mars environment
- Draped nature of IMF about Martian obstacle "channels" magnetosonic waves into nightside ionosphere
- Adiabatic and nonadiabatic wave-particle interaction processes heat light and heavy planetary ions

Correspondence to:
C. M. Fowler,
christopher.fowler@mail.wvu.edu

Citation:
Fowler, C. M., Hanley, K. G., McFadden, J. P., Chaston, C. C., Bonnell, J. W., Halekas, J. S., et al. (2021). MAVEN observations of low frequency steepened magnetosonic waves and associated heating of the Martian nightside ionosphere. *Journal of Geophysical Research: Space Physics*, *126*, e2021JA029615. https://doi.org/10.1029/2021JA029615

Received 1 JUN 2021
Accepted 29 SEP 2021

MAVEN Observations of Low Frequency Steepened Magnetosonic Waves and Associated Heating of the Martian Nightside Ionosphere

C. M. Fowler[1,2], K. G. Hanley[1], J. P. McFadden[1], C. C. Chaston[1], J. W. Bonnell[1], J. S. Halekas[3], J. R. Espley[4], G. A. DiBraccio[4], S. J. Schwartz[5], C. Mazelle[6], D. L. Mitchell[1], S. Xu[1], and R. J. Lillis[1]

[1]Space Sciences Laboratory, University of California, Berkeley, CA, USA, [2]Department of Physics and Astronomy, West Virginia University, Morgantown, WV, USA, [3]Department of Physics and Astronomy, University of Iowa, Iowa City, IA, USA, [4]NASA Goddard Space Flight Center, Greenbelt, MD, USA, [5]Laboratory for Atmospheric and Space Physics, Boulder, CO, USA, [6]IRAP, University of Toulouse-CNRS-UPS-CNES, Toulouse, France

Abstract We present Mars Atmosphere and Volatile EvolutioN (MAVEN) observations of low frequency steepened fast magnetosonic waves in the Martian magnetosphere and ionosphere. Solar wind pressure pulses generated in the upstream foreshock region impact the magnetopause and generate the magnetosonic waves within the magnetosphere, in a process analogous to the production of magnetic Pc pulsations in the terrestrial magnetosphere. The draped nature of the IMF about Mars, combined with the near-perpendicular propagation of these waves across the magnetic field, act to channel these waves into the nightside ionosphere, where they are observed in their non-linear steepened form. Coincident-in-time ion observations show that the light (H^+) and heavy (O^+, O_2^+, CO_2^+) planetary ion distribution functions possess significant suprathermal energetic tails, arising from wave-particle interactions with the steepened waves. The short gyro period and small gyro radius of the protons, relative to the steepened waves, results in proton heating via adiabatic compression. In contrast, the long gyro period of the heavy ions relative to the wave frequency leads to nonadiabatic heating via wave-trapping processes. The light and heavy ion species are heated above escape energy by these waves, even down close to the exobase. A limited statistical study of 101 neighboring orbits found that similar wave events occurred on 28% of orbits analyzed, suggesting that such wave-heating events may be important drivers of the Mars nightside ionospheric dynamics and energy budget. Our discussion includes placing our results in the context of solar wind energy transfer to the ionospheres of unmagnetized and magnetized bodies in general.

1. Introduction

Electromagnetic waves are an important component of collisionless space plasma environments because they can carry energy and momentum and deposit it into different plasma regions via interactions with charged particles. The magnetospheres and upper ionospheres of planets are collisionless environments where charged particle motion is controlled by electromagnetic forces, and electromagnetic waves are known to play important roles in the transport of energy in these regimes (Cravens, 2004; Schunk & Nagy, 2009). The types of electromagnetic wave modes that exist in planetary magnetospheres depend upon the size, structure, and nature of the magnetospheres themselves, which are in turn driven in large part by whether the bodies in question possess significant intrinsic global dipole magnetic fields or not. Strongly magnetized bodies, such as Earth, possess strong dipole fields that stand off the impeding solar wind at relatively large distances upstream of the body (typically 10's or more planetary radii, Fairfield, 1971; Jackman et al., 2019). In contrast, unmagnetized bodies such as Mars, Venus, and comets do not possess strong global dipole fields and the solar wind can interact directly with their gravitationally bound ionospheres. This interaction drives electrical currents within the ionospheres, leading to induced magnetospheres that stand off the solar wind at much closer distances to the bodies (typically 1–2 planetary radii, Vignes et al., 2000; Zhang, Luhmann, & Russell, 1990) and that are characterized to first order by a "draped" magnetic field configuration rather than the dipole structure of their magnetized counterparts (Bertucci et al., 2011; Brain et al., 2006; Halekas et al., 2017).

Low-frequency waves generated in the vicinity and upstream of the bow shocks of unmagnetized bodies can have wavelengths comparable to the length scale of the bow shock-upper ionosphere stand off distance, and it has long been predicted that these electromagnetic waves can interact directly with the upper ionospheres to deposit energy there via wave-particle interactions (Ergun et al., 2006; Moses et al., 1988). Indeed, studies of the Martian and Venusian ionospheres have shown that topside heat fluxes, postulated to arise from this "wave heating," are required to obtain agreement between photochemical models and observations of these ionospheres. These topside heat fluxes influence dayside upper ionospheric energy balance, structure and dynamics (Chen et al., 1978; Choi et al., 1998; Cui et al., 2015; Cravens et al., 1980; Matta et al., 2014; Scarf et al., 1980; Shapiro et al., 1995).

A variety of electromagnetic wave modes are generated in the vicinity of the shocks of unmagnetized planets (Brain et al., 2002; Espley et al., 2004; Ruhunusiri et al., 2015). This study focuses on fast magnetosonic waves at Mars, their propagation from shock vicinity to ionosphere, and their subsequent impact on the Martian ionosphere via wave-particle interactions. Fast magnetosonic waves are typically low frequency, compressional wave modes that propagate perpendicular to the magnetic field and are observed as fluctuations in the magnetic field amplitude (Baumjohann & Treumann, 2012). Magnetosonic waves are observed in a variety of laboratory and space plasma environments, including tokamak experiments (Jacquinot et al., 1977; Karney et al., 1979), unmagnetized planetary magnetospheres (Mazelle et al., 2004; Shan et al., 2014; Shan, Ge, & Du, 2020), comets (Tsurutani et al., 1987, 1989) and magnetized planetary magnetospheres (Cramm et al., 1998; Glassmeier, 1995; Kepko & Spence, 2003).

In their linear form, the magnetosonic wave fluctuations are quasi-sinusoidal in nature. These waves can evolve to a non-linear state known as steepened magnetosonic waves, whereby the wave fluctuations take on a "sawtooth" like appearance. This evolution arises due to differences in the wave phase speed across a single wave cycle (Matsumoto & Nagai, 1981; Omidi & Winske, 1990; Tsurutani et al., 1987). Kinetic simulations have shown that linear and steepened magnetosonic waves can heat ambient plasma under a variety of plasma conditions: Landau damping of electrons (Matsumoto & Barnes, 1982; Matsumoto & Nagai, 1981); ion heating via cyclotron subharmonic resonance ($\omega < \omega_{ci}$) (Terasawa and Nambu, 1989); and nonresonant ion heating ($\omega > \omega_{ci}$) (Lembege et al., 1983; Lembege & Dawson, 1984). Here, ω is the magnetosonic wave frequency and ω_{ci} is the cyclotron frequency of the heated ion species.

In the case of unmagnetized bodies (in particular Mars and Venus), observations have shown that quasi-monochromatic magnetosonic waves can be generated upstream of the bow shocks in both their linear and steepened forms, that in some cases can propagate through to the underlying magnetosheath (Shan et al., 2014; Shan, Du, et al., 2020; Shan, tsurutani, et al., 2020). In addition, Collinson et al. (2018) demonstrated that ultralow frequency (ULF) magnetosonic waves could be driven in the Martian magnetosphere via pressure pulsations generated in the upstream region that were advected back into the magnetopause boundary. The impact of these pressure pulses with the magnetopause boundary lead to a "ringing" of the magnetosphere at the same frequency as these impacts. This process was suggested to be analogous to the generation of magnetic Pc pulsations in the terrestrial magnetosphere, characterized as standing waves in the form of ULF toroidal and poloidal oscillations of the dipole field (Farrugia et al., 1989; Glassmeier et al., 2004; Sibeck et al., 1989). Sources of these upstream pressure pulses at Earth include pressure variability within the solar wind (Kepko & Spence, 2003) and instabilities that arise in the ion foreshock region from ions reflected at the shock front (Eastwood et al., 2005). In addition, the smaller magnetospheres of Venus and Mars mean that pressure pulsations can also be generated in the vicinity of the planetary shocks via the generation of waves resulting from the solar wind pickup of newly ionized planetary hydrogen Shan, Du, et al. (2020); Shan, tsurutani, et al. (2020).

Ionospheric joule heating is known to be a major process in the damping of magnetic Pc pulsations at Earth (Glassmeier et al., 1984; Lathuillere et al., 1986), and plasma observations at Mars have provided evidence that these analogous ULF magnetosonic wave events can also be damped by heavy ions in the planetary ionosphere (Collinson et al., 2018; Fowler et al., 2018). Su et al. (2020) further demonstrated that electron Landau resonance with these ULF waves can drive significant electron heating in the Martian ionosphere. In contrast to Earth, the relatively low gravitational potential of Mars means that this ionospheric damping appears capable of driving significant changes to ionospheric dynamics and enhancing ion escape rates to space, through both the direct heating of planetary ions and the creation of ambipolar electric fields via

the electron heating. Our understanding of the processes that generate these waves and that govern their interaction with unmagnetized planetary ionospheres is still relatively limited: although recent case studies have demonstrated that such interactions occur, the impacts on the ionospheres of unmagnetized bodies are not fully understood nor characterized.

Low frequency fast magnetosonic waves have also been observed in the near space environment of comet Giacobini-Zinner, another unmagnetized body exposed to the super sonic solar wind flow. These waves displayed both quasi-linear and steepened characteristics, originating via the right hand resonant ion ring beam instability due to the solar wind pickup of water group ions in the vicinity of the comet (Tsurutani et al., 1987, 1989). These magnetosonic waves have been observed in greater abundance when the comet is more active (Ostaszewski et al., 2020). Hybrid simulations have confirmed that the steepened waves evolve from their linear counterpart, and have demonstrated that the steepened waves observed upstream of the comet act in a similar fashion to subcritical dispersive shocks, in that they can heat and decelerate the solar wind to subsonic speeds (Omidi & Winske, 1990).

While linear magnetosonic waves have been observed in the Martian magnetosphere and shown to propagate into the dayside ionosphere where they can heat planetary ions via wave-particle interactions (Collinson et al., 2018; Fowler et al., 2018), to our knowledge the impact of the non-linear steepened variety on the Martian ionosphere has not been reported before. We present here a case study of non-linear steepened magnetosonic waves that propagate from their point of creation (the magnetopause) to the nightside ionosphere, where significant heating of planetary ions is observed coincident with these waves. We demonstrate that various wave-particle interaction processes facilitate this ion heating, and discuss the broader implications of this event in the context of unmagnetized bodies in general.

The remainder of this paper is organized as follows: the MAVEN data analyzed in this study are described in Section 2 and we provide an overview description of the case study event in Section 3. A detailed analysis of the event is presented in Section 4 and we present our discussion and interpretation of the results in Section 5. We present the results of a small statistical study of similar magnetosonic wave events in Section 6 before concluding in Section 7.

2. Datasets Analyzed

The data analyzed in this study are from NASA's Mars Atmosphere and Volatile EvolutioN (MAVEN) mission, which entered Mars orbit in the fall of 2014 (Jakosky et al., 2015). MAVEN's orbit is elliptical in nature, with a periapsis that typically sampled altitudes down to ~150 km and an apoapsis of ~6,000 km, allowing it to regularly sample the upstream solar wind. In mid February 2019 MAVEN's periapsis (apoapsis) altitude was raised (lowered) to altitudes of ~200 (~4,500) km in order to conserve fuel and extend the mission lifetime. This study utilizes data from the plasma instruments carried by MAVEN, namely SupraThermal And Thermal Ion Composition (STATIC, McFadden et al., 2015); Magnetometer (MAG, Connerney, Espley, Lawton, et al., 2015) and Solar Wind Ion Analyzer (SWIA, Halekas et al., 2015). Data from these instruments are obtained from the NASA Planetary Data System (PDS).

STATIC is a top-hat electrostatic analyzer that uses time of flight to distinguish ion mass. It measures ions of energies below 1 eV up to 30 keV, using electrostatic deflectors to obtain a field of view of 360° × 90°. The STATIC "c6" data products are used in this study, which consist of ion distribution functions as a function of energy and mass dimensions obtained at 4 s cadence. Ion densities and temperatures used in this study were provided by the STATIC instrument team.

MAG consists of two fluxgate magnetometers that each measure the 3D magnetic field vector at 32 Hz. The two fluxgates provide hardware redundancy and allow for the calibration and removal of spacecraft generated magnetic fields (Connerney, Espley, DiBraccio, et al., 2015). The instrument can measure magnetic fields up to 65,536 nT in strength at an accuracy better than 0.05%. Publicly available software written by the MAG instrument team is used to produce magnetic field wavelet power spectra, based on the process outlined in Torrence and Compo (1998). The 3D magnetic field vectors are presented in the Mars Solar Orbital (MSO) coordinate system in this paper, defined as X pointing Sunward along the Mars-Sun line; Y pointing

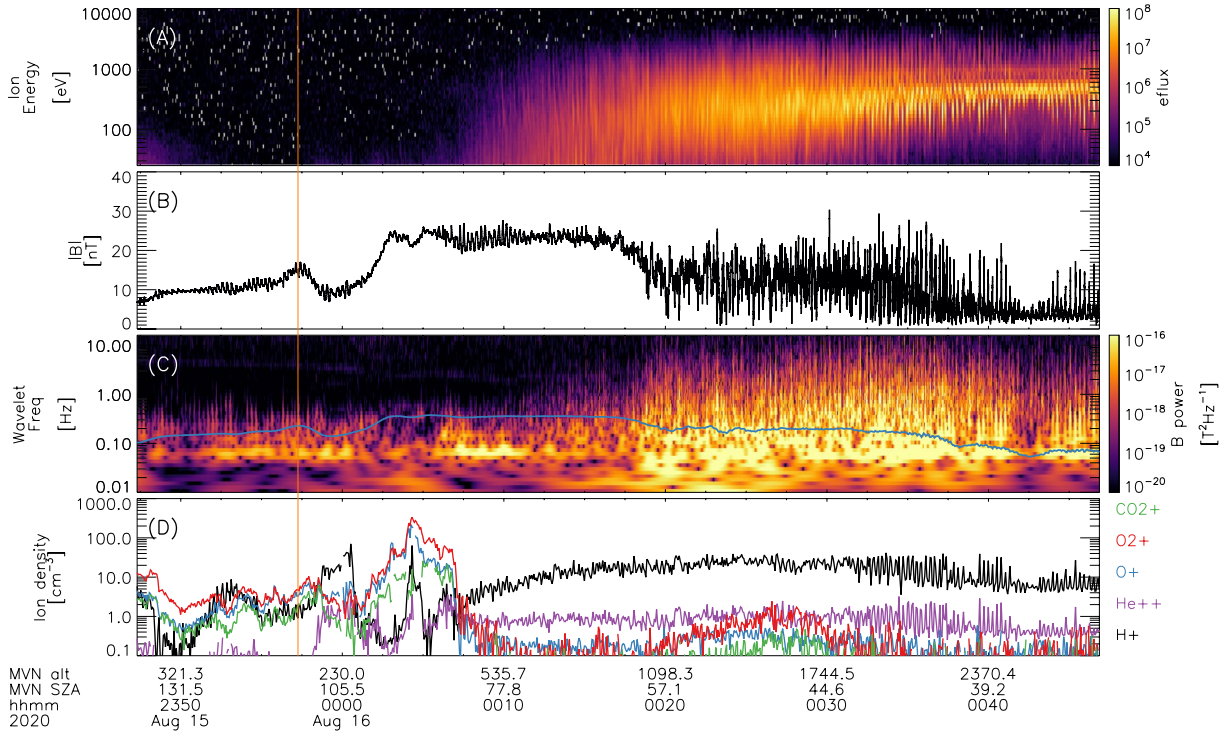

Figure 1. MAVEN overview observations of the case study analyzed. Panels show: (a) SWIA ion energy spectrogram, (b) magnetic field amplitude, (c) wavelet Fast Fourier Transform (FFT) of panel (b) with proton gyro frequency over plotted in blue, (d) ion densities measured by STATIC. Eflux has units of eV (eV s sr cm^2)$^{-1}$. Periapsis is marked by the orange vertical line. The spacecraft solar zenith angle (SZA) and altitude (alt) are printed underneath the bottom panel in units of degrees and kilometers, respectively.

opposite to Mars' orbital motion in the ecliptic plane, and Z completing the right-handed system pointing north out of the ecliptic plane.

SWIA is an electrostatic top hat analyzer designed to measure the solar wind. The instrument field of view, provided by electrostatic deflectors, spans 360° × 90°. SWIA measures ion fluxes from 25 eV up to 25 keV in energy, with an energy resolution of 14.5%. The data presented here have a cadence of 4 s.

3. Overview of Event

This section provides a qualitative overview of the event studied in this manuscript, while Section 4 provides more detailed quantitative analysis. The time series plasma data shown in Figure 1 span a MAVEN periapsis pass and outbound orbit segment. Data are shown from the SWIA, MAG, and STATIC instruments, along with the spacecraft altitude and solar zenith angle (SZA) underneath the plot. Describing the figure from right to left (i.e., "backwards" in time), MAVEN is upstream of the bow shock sampling disturbed solar wind at times after 00:40 UTC. The ion density is dominated by solar wind protons and alpha particles (H^+ and He^{++}). Moving backwards in time, MAVEN observes highly disturbed and turbulent conditions in the particle and magnetic field data between 00:20 and 00:40 UTC. The shocked ion populations (i.e., ions observed across a wide range of energies by SWIA) combined with the turbulent conditions (i.e., large amplitude, high frequency fluctuations in SWIA, MAG, and STATIC) are indicative of MAVEN sampling the upstream foreshock region, formed when the solar wind interplanetary magnetic field (IMF) is magnetically connected to the shock front (e.g., Schwartz & Burgess, 1991). The wavelet power spectrum shows significant wave power across a range of frequencies within the magnetosheath and foreshock regions, which is a common characteristic of these regions (e.g., Brain et al., 2002; Espley et al., 2004). Of particular interest for this study is the peak in wave power observed at ~0.06 Hz throughout most of the time range covered by the figure, including the periapsis pass within the ionosphere.

MAVEN samples the magnetic pileup region between about 00:10 and 00:20, marked by the increase in the magnetic field strength and reduction in shocked ions observed by SWIA. Quasi-sinusoidal compressive magnetosonic waves are observed in the magnetic field strength, particularly around 00:10, and these waves appear to damp (amplitude decreases) as MAVEN samples the dense, cold planetary ionosphere at ~00:07 (marked by the sudden increase in heavy planetary ion densities, O^+, O_2^+, and CO_2^+, panel d). The interpretation of wave damping is further highlighted by the decrease in wave power (panel C) at the 0.06 Hz band at this time. Periapsis occurs on the nightside at a SZA of 113° (marked by the vertical orange line), and MAVEN observes compressive waves in the magnetic field data surrounding periapsis. As we shall demonstrate, these waves at periapsis are steepened magnetosonic waves that are observed coincident with heated planetary ions. Our hypothesis is that the low frequency waves observed upstream are associated with pressure pulses that are advected back into the magnetopause by the solar wind flow. The impact of these pressure pulses with the magnetopause 'rings' the magnetosphere in a fashion similar to the generation of magnetic Pc pulsations at Earth, driving compressive, magnetosonic waves at the same frequency within the magnetosphere. These low frequency magnetosonic waves propagate into the ionosphere, where wave-particle interactions lead to wave damping and planetary ion heating. The following sections provide more detailed analysis that support these interpretations.

4. Detailed Analysis

The following section provides a detailed analysis on various aspects of the event shown in Figure 1. We start with a brief discussion of the likely wave generation mechanisms in the upstream region, before focusing on the interaction between the observed magnetosonic waves and the ionosphere.

4.1. Upstream Wave Generation

MAVEN observations of the upstream region are shown in Figure 2. Wave polarization analysis using the methods described in Chaston et al. (1998); Samson and Olson (1980) was carried out on the 3D magnetic field measurements, providing wave power, polarization, wave normal angle (WNA - the angle at which the wave propagates relative to the local magnetic field) and ellipticity, as a function of time and wave frequency. By extracting these parameters at the peak in wave power observed at ~0.06 Hz, we are able to determine the properties and wave mode of the observed low frequency waves (for the remainder of this manuscript, we will refer to these waves as "the 0.06 Hz waves"). The black line in Figure 2d marks the frequency of peak wave power, which was determined by an automated peak-finding algorithm. The blue line in the panel shows the proton gyro frequency. The extracted wave parameters at this peak frequency are shown in panels (e–h) of the figure. Upstream of the shock front, at times after ~00:40, the 0.06 Hz waves are left-hand elliptically polarized in the spacecraft frame propagating obliquely to the magnetic field, at the proton gyro frequency.

As MAVEN encounters what is likely the quasi-parallel shock front between 00:30 and 00:40 (marked by the increase in magnetic field strength, large amplitude fluctuations, and rotation in the magnetic field to a draped configuration), the 0.06 Hz waves shift from obliquely to perpendicularly propagating waves (WNA changes from ~40° to ~80°). The ellipticity of the waves shifts from near left hand ellipticity ($-1 <$ ellipticity < 0) to values that are more linearly polarized (ellipticity closer to 0, values of ~−0.2 to −0.4) in nature. These characteristics mark these perpendicularly propagating waves as compressive fast magnetosonic waves, and clear quasi-sinusoidal, large amplitude fluctuations in the magnetic field amplitude (consistent with fast magnetosonic waves) are observed centered around 00:10 and also at times centered around periapsis. These low frequency quasi-sinusoidal wave forms are not as obvious in the magnetosheath region (~00:20–00:40) due to the presence of additional wave-like variations that span the full frequency spectrum and "smear-out" the 0.06 Hz waves (e.g., panels c and d).

Our interpretation of these observations is as follows: the 0.06 Hz left hand elliptically polarized (in the spacecraft frame) waves are generated upstream of Mars by ion instabilities resulting from the pickup of newly ionized planetary hydrogen or back streaming ions reflected at the shock (Collinson et al., 2018; Mazelle et al., 2004; Shan, Ge, & Du, 2020; Shan, Du, et al., 2020). These processes are not mutually exclusive and both may contribute to the observed conditions here. These waves are right handed in nature and

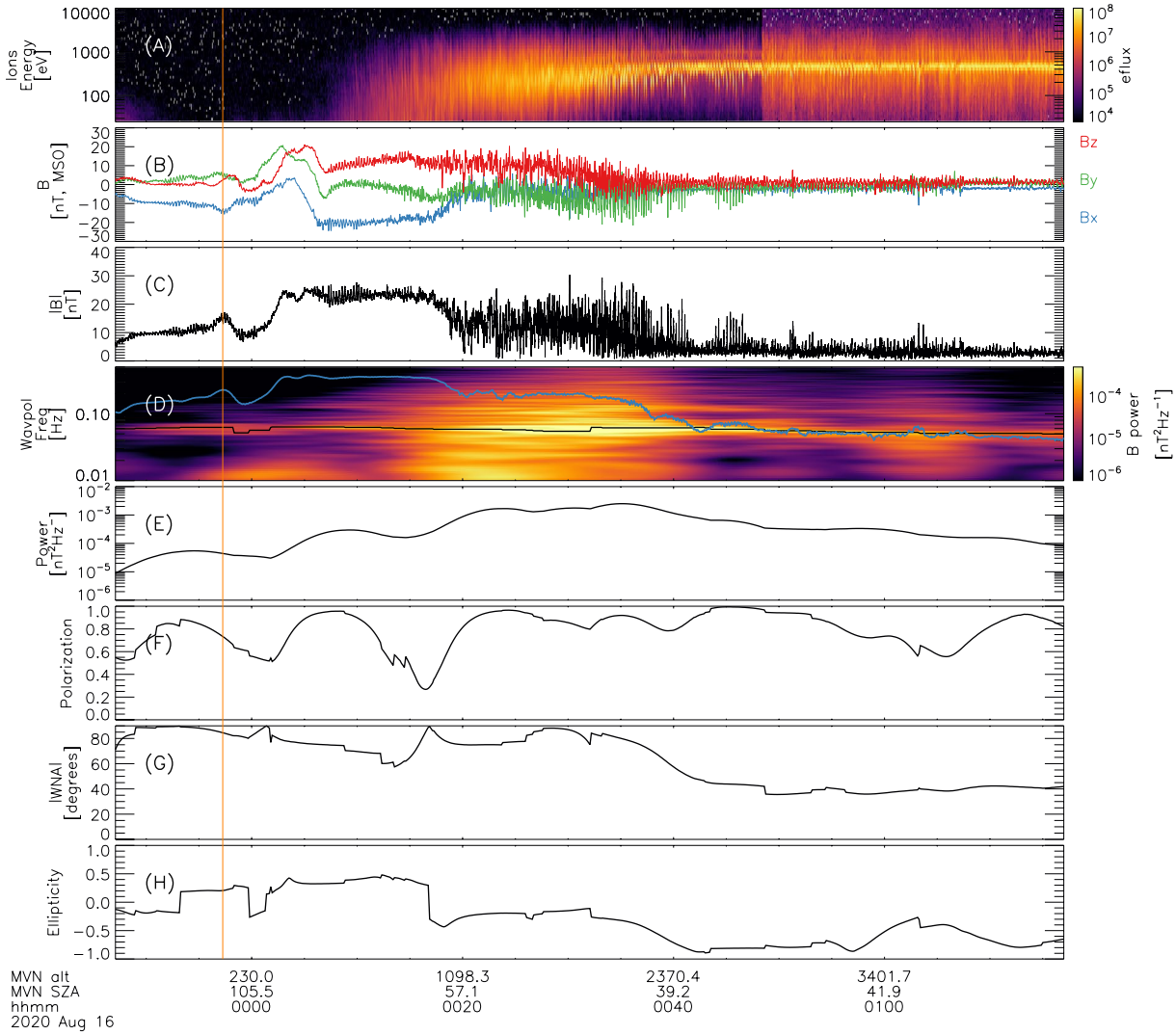

Figure 2. Time series plasma data spanning the periapsis pass up to the generation region of the observed low frequency magnetosonic waves. Panels show: (a) SWIA ion energy spectrum; (b) 3D magnetic field vector; (c) magnetic field amplitude; (d) wavelet FFT from wave polarization analysis; blue marks the proton gyro frequency and black marks the peak wave power of the 0.06 Hz waves; (e–h) wave polarization analysis results extracted at the peak wave power noted above: wavelet FFT power, polarization, absolute wave normal angle, and ellipticity. Values of polarization greater than ~0.7 are typically considered "coherent" wave structures. The orange vertical line marks periapsis.

typically propagate in the sunward direction, however, their group velocities are usually much less than the solar wind velocity, resulting in the waves being advected back into the shock and being observed as left handed in the spacecraft frame (Tsurutani et al., 1987). Pressure pulses accompany these waves, and as they impact the magnetopause they "ring" the magnetosphere in a fashion analogous to the generation of magnetic Pc pulsations at Earth (e.g., Farrugia et al., 1989; Sibeck et al., 1989). This ringing of the magnetopause generates compressive, fast magnetosonic waves at a frequency similar to the driving pulses that are able to propagate within the magnetosphere. Such a process has recently been suggested to be active at Mars by Collinson et al. (2018). The draped nature of the IMF about the planetary obstacle (which is discussed in Section 5) results in these fast magnetosonic waves propagating toward the planetary ionosphere. As already noted, the focus of this paper is to determine the effects that these fast magnetosonic waves have on the ionosphere, and we leave a detailed analysis of the wave generation mechanisms for a future study.

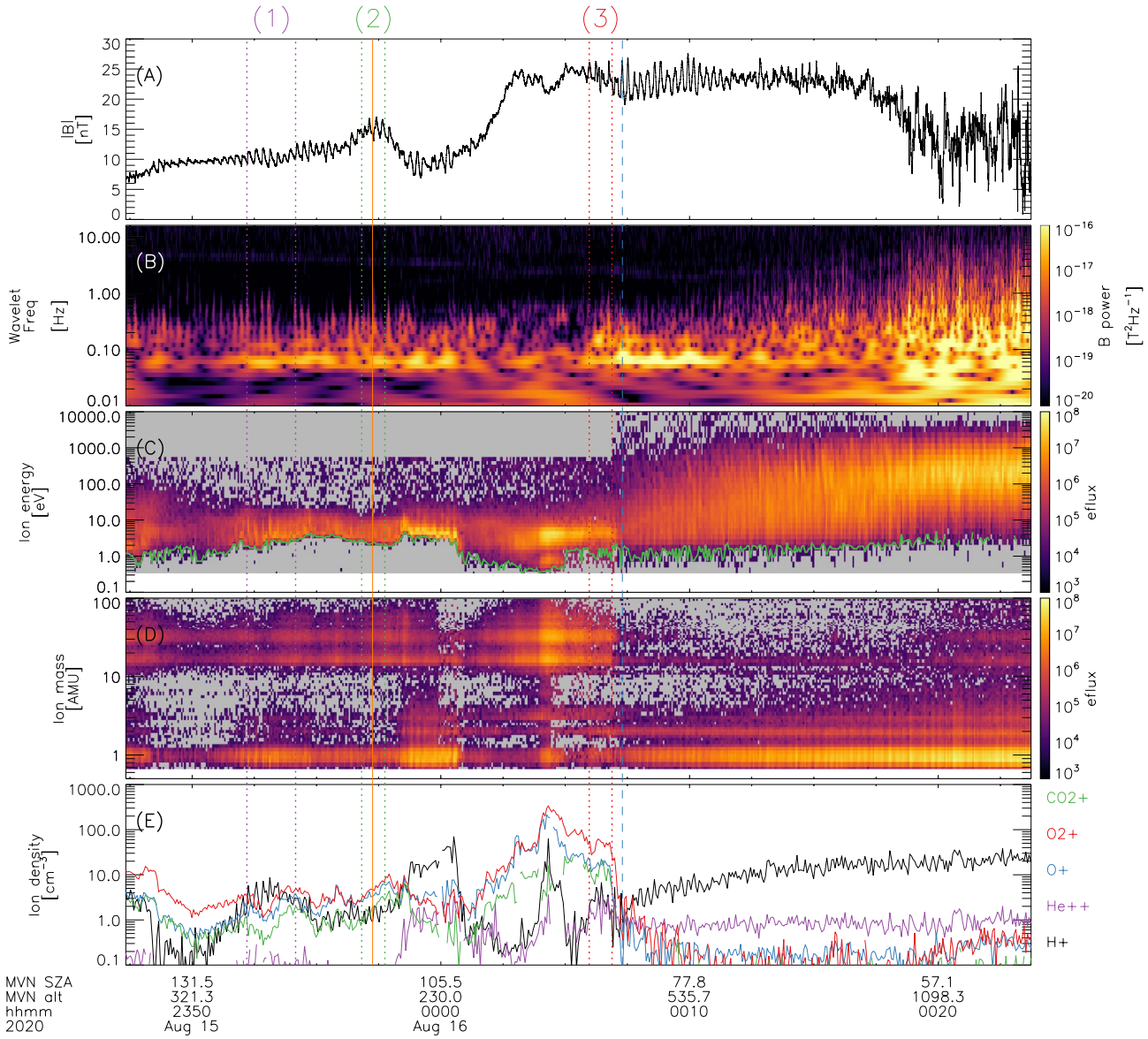

Figure 3. Time series plasma data focused on the observation of magnetosonic waves in the ionosphere. Panels show: (a) magnetic field amplitude; (b) wavelet FFT of panel (a); (c) STATIC ion energy spectrum for all ions; (d) STATIC ion mass spectrum; (e) ion densities derived from STATIC data. The blue dashed vertical line marks the location of the upper ionosphere (where heavy planetary ion densities dominate the plasma composition). The regions labeled 1–3 are analyzed in further detail and discussed in the main text. Eflux has units of eV (eV s sr cm^2)$^{-1}$.

4.2. Wave Damping and Heated Ionospheric Ions

A zoom in on the periapsis pass is shown in Figure 3, which includes ion energy and mass spectra observed by STATIC (panels c and d, respectively). The green line in panel C marks the negative spacecraft potential as measured by STATIC, which is a few volts negative for this periapsis pass. These values are typical and the STATIC energy spectrum has not been corrected for spacecraft potential effects. The dashed blue vertical line marks the location of the upper ionosphere, where the ion density switches from predominately heavy ions (O^+ and O_2^+) to solar wind/sheath (H^+ and He^{++}) dominated. This switch is visible in the STATIC data panels (c), (d), and (e): relatively cold low energy heavy plasma dominates within the ionosphere, while hot shocked H^+ and He^{++} dominate above this.

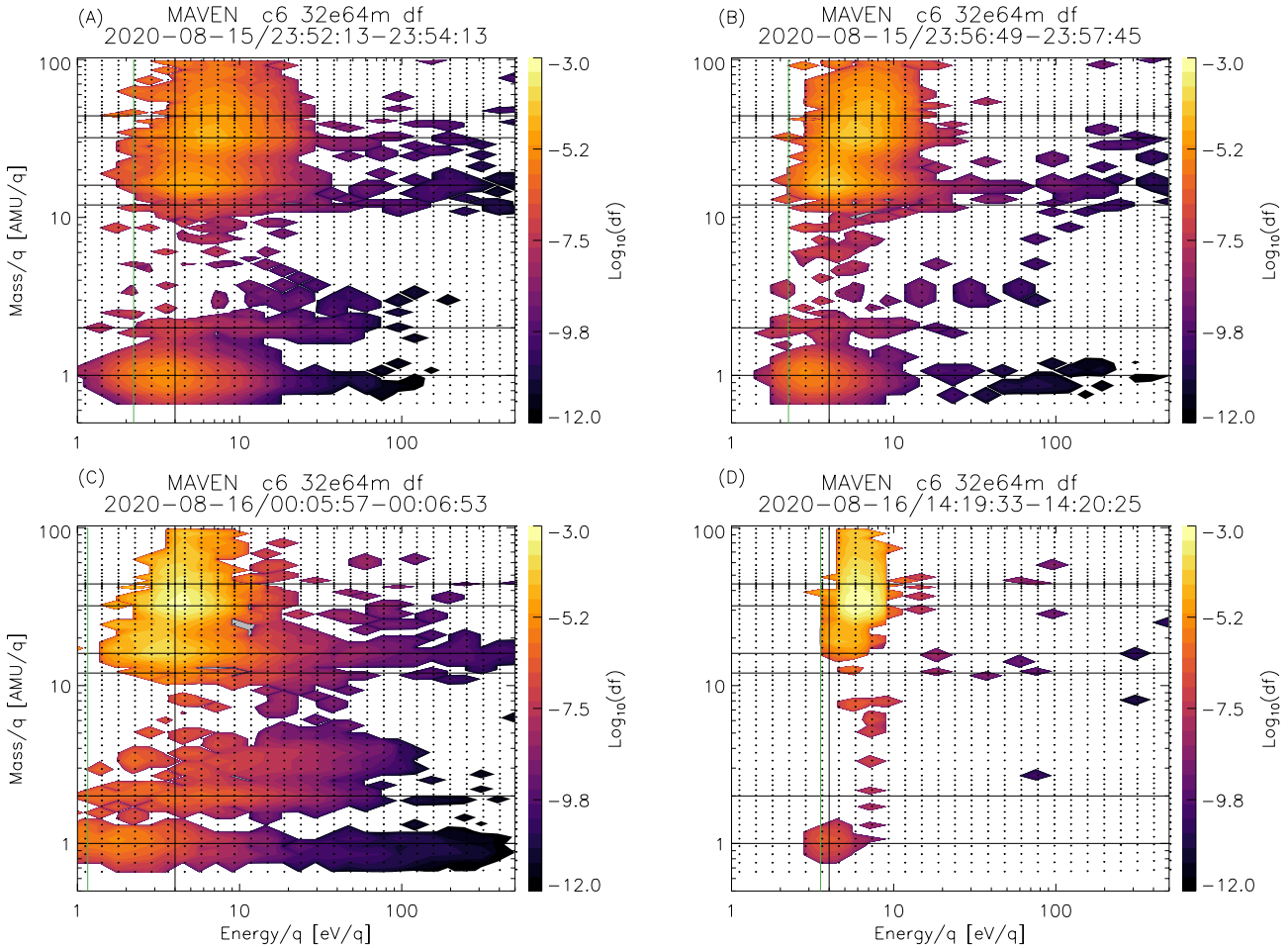

Figure 4. Ion distribution functions (IDFS) measured by STATIC. Panels (a), (b), and (c) correspond to time periods 1, 2, and 3 in Figure 3. Panel (d) is measured during a later periapsis pass when wave activity was not present, showing more typical IDFS during cold ionospheric conditions. The colored contours denote distribution function in units of $(km^3\ s^{-3}\ cm^3)^{-1}$. The green line marks the spacecraft potential as measured by STATIC, the black line marks 4 eV for reference. IDFS have not been corrected for spacecraft potential or spacecraft RAM effects. Low eflux "speckle" is likely noise and should not be considered statistically significant for this study.

The quasi-sinusoidal fast magnetosonic waves identified by the wave polarization analysis are clearly visible in the magnetic field amplitude and wavelet spectrum (panels a and b) at and just prior to 00:10. Close inspection shows that the wave amplitudes in panel (a) vary in phase with observed solar wind/sheath H^+ and He^{++} densities in panel (e), further supporting the interpretation that these low frequency waves are fast magnetosonic in nature. Between midnight and the blue dashed vertical line, relatively little wave power at 0.06 Hz is observed, a characteristic confirmed by the lack of large amplitude variations in the magnetic field strength (panel a). Additional significant wave power is observed centered around and prior to periapsis and these waves are characterized by a sawtooth like form (panel a), marking them as steepened magnetosonic waves (a characteristic that we confirm in Section 4.4).

Ion distribution functions (IDFS) measured by STATIC are shown as functions of energy and mass from the three time periods marked in Figure 3 (marked by the pairs of dotted vertical lines and labeled 1–3) in Figure 4. Figure 4a shows the average IDFS observed over time period 1; the vertical axis denotes mass divided by charge (m/q), where horizontal lines mark typically important ion species at Mars with $m/q = 1$, 2, 12, 16, 32, and 44. These correspond to H^+, He^{++} or H_2^+, C^+, O^+, O_2^+, CO_2^+, respectively. As discussed in McFadden et al. (2015), the presence of H_2^+ versus He^{++} can be determined by the presence of a "ghost peak" at m/q ~11. The presence of this peak in panel (a) suggests that the ions observed at $m/q = 2$ are H_2^+

for the shown time period. The relatively low energies ($\lesssim$50 eV) of the observed ions marks them as planetary in nature, with perhaps a small contribution of sheath protons observed at higher energies for $m/q = 1$.

The distribution functions of the major ionospheric species during time period 1 (H^+, O^+, and O_2^+, Figure 4) all possess elongated tails in the energy dimension. This characteristic is known as a suprathermal tail and is typically associated with ion heating. The steepened magnetosonic waves that are observed coincident in time are a likely source of this heating, which will be discussed in Section 4.3. These suprathermal tails extend up to ~15–20 eV in energy (after corrections for spacecraft potential and velocity), which is well above the escape energy of ~2 (4) eV for O^+ (O_2^+) at Mars. The observed ion heating may thus be a driver of atmospheric escape to space, and this is discussed in more detail in Section 6.

IDFS observed during time period 2 (periapsis, 213 km altitude) are shown in Figure 4b. Suprathermal tails are also present for the major ionospheric species, albeit extending out to slightly lower energies, ~15 eV or so. The coincident presence of magnetosonic waves again strongly suggests the role of wave-particle interactions driving this heating, and these observations demonstrate that planetary ions are significantly heated down to periapsis during this periapsis pass.

The IDFS presented in Figure 4c are observed during time period 3, at the upper ionosphere boundary. During this time period a combination of planetary and solar wind/sheath populations are observed by STATIC. Solar wind/sheath protons are observed at energies above ~30 eV, while protons of planetary origin are observed at lower energies. Heavy planetary ions (in particular O^+, O_2^+, and CO_2^+) are the dominant ion species, although significant H_2^+ is present, again inferred from the ghost peak at $m/q \sim 11$. Significant suprathermal tails exist for the heavy planetary ions reaching energies of several 10's eV. During this time period the quasi-sinusoidal magnetosonic wave amplitudes damp, suggesting that stochastic-like heating of the planetary ions occurs, similar to that reported by Fowler et al. (2018). Further analysis in Section 4.3 supports this interpretation.

Figure 4d shows IDFS observed by STATIC during a later periapsis pass (similar altitude to panel B) when wave activity was not present and ionospheric conditions were representative of more typical "quiet time" conditions. The IDFS are notably more Maxwellian in shape and lack significant suprathermal tails in the energy dimension. Panel (d) provides context and demonstrates that the IDFS observed during periods 1–3 are significantly altered in shape compared to quiet time conditions when wave activity is not present.

4.3. Wave-Particle Interactions

We have so far postulated that the observed magnetosonic and steepened magnetosonic waves heat planetary ions via wave-particle interactions. A more detailed analysis presented in this section provides support for this hypothesis and insight into the physical mechanisms at play. A variety of plasma parameters associated with the observed magnetosonic waves and planetary ions are shown in Figure 5. These parameters are calculated using the MAVEN observations, and we discuss how they are obtained here.

4.3.1. Magnetosonic Wave Dispersion Relation and Basic Wave Properties

We start with the dispersion relation for a fast magnetosonic wave, which is given by Equation 1 (Schunk & Nagy, 2009):

$$\omega^2 = k^2 \frac{V_S^2 + V_A^2}{1 + \frac{V_A^2}{c^2}} \tag{1}$$

where k is the wave number; V_S is the sound speed, V_A is the Alfvén speed and c is the speed of light in a vacuum. V_S is defined as $\sqrt{\frac{\gamma k_b T_e}{m_i}}$; V_A as $\sqrt{\frac{B}{\mu_0 \rho}}$; where γ is $\frac{5}{3}$ for a monatomic gas and $\frac{7}{5}$ for a diatomic gas, k_b is the Boltzmann constant; T_e is the electron temperature, m_i is the ion mass; B is the magnitude of magnetic field strength, μ_0 is the permeability of free space; and ρ is the mass density, defined as $\sum_i n_i m_i$, where n_i is the ion density, and the subscript i refers to each ion species.

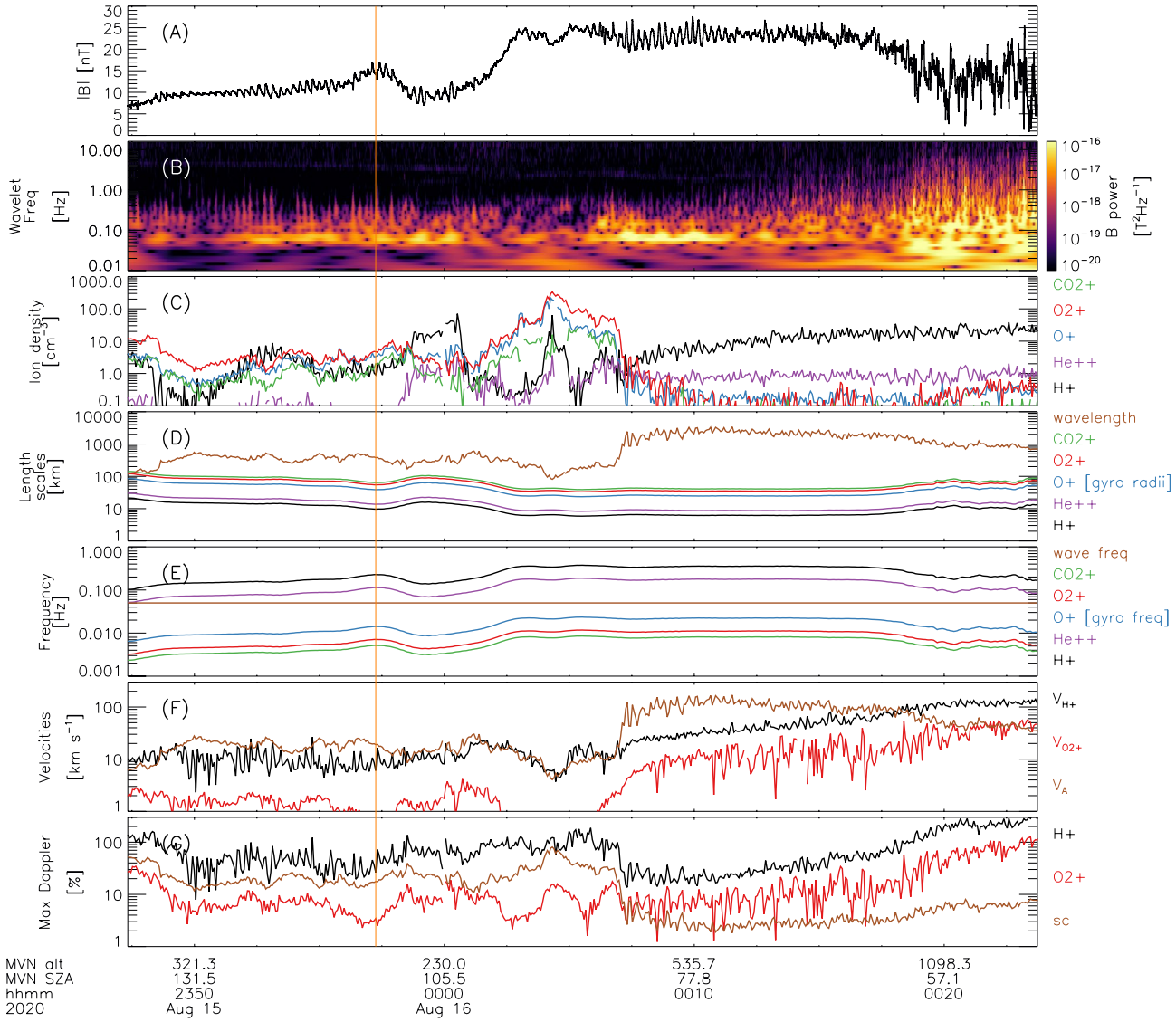

Figure 5. Time series plasma data of various plasma parameters derived from the MAVEN observations. Panels show: (a) magnetic field amplitude; (b) wavelet FFT of panel (a); (c) ion densities derived from STATIC observations; (d) relevant length scales (magnetosonic wave length and ion gyro radii); (e) relevant time scales (magnetosonic wave frequency and ion gyro frequencies); (f) relevant velocities: the local Alfvén speed and the H^+ and O_2^+ flow velocities (corrected for spacecraft potential and spacecraft velocity effects); (g) the maximum percentage change in observed magnetosonic wave frequency (in the spacecraft frame) due to Doppler shift, resulting from the spacecraft motion and ion flows.

V_A is calculated using the observed magnetic field strength and ion densities; we assume that the plasma is composed primarily of H^+, He^{++}, O^+, O_2^+, and CO_2^+. The resulting V_A is shown in Figure 5f: within the sheath and solar wind V_A reaches several tens to ~100 km s^{-1}, while in the dense ionosphere V_A is 10–20 km s^{-1}. For comparison, the MAVEN spacecraft velocity is ~2 and ~4 km s^{-1} at apoapsis and periapsis respectively.

An estimate of V_S can be obtained based on the MAVEN observations. MAVEN carries a Langmuir Probe instrument (Langmuir Probe and Waves, LPW, Andersson et al., 2015) that provides measurements of the thermal electron density and temperature, however, these moments are unavailable for this particular pass. By assuming that the electron temperature T_e is twice the O_2^+ temperature, T_e ~ 2000 K, we obtain an estimate of $V_S \lesssim 1$ km s^{-1}. This assumption is based upon recent comparisons made between ion and electron temperatures measured by MAVEN (Hanley et al., 2020). Thus, at all times in this pass, V_S is at least an order of magnitude smaller than V_A, and, using the fact that $c \gg V_A$, we can approximate Equation 1 by:

$$\omega \approx kV_A \tag{2}$$

The group velocity of the magnetosonic waves is defined as $V_g = \frac{\partial \omega}{\partial k} = V_A$, and an estimate of the magnetosonic wavelength is obtained via $\lambda_{MS} = \frac{V_A}{f}$, where $f = 0.06$ Hz. As we show in Section 4.3.2, the compressive waves in the solar wind and magnetosheath regions are likely to be heavily Doppler shifted as they are advected into the shock by the solar wind. As such, the estimated wavelength represents a lower limit within the magnetosheath and solar wind regions. A comparison of the magnetosonic wavelength to the ion gyro radii is shown in Figure 5d. The ion gyro radii are calculated by assuming that the ion velocity perpendicular to the magnetic field, V_{perp}, is equivalent to the observed O_2^+ ion temperature, that is, $V_{perp} = \sqrt{\frac{2E}{m_i}}$, where $E = 0.1$ eV, equivalent to a temperature of ~1000 K. The magnetosonic wavelength is 1,000–2,000 km in the sheath and solar wind, and shortens to several hundred km in the denser ionosphere. The light ion (H^+ and He^{++}) gyro radii are at least an order of magnitude smaller than the magnetosonic wavelength throughout the entire pass. The heavier ion (O^+, O_2^+, and CO_2^+) gyro radii are also smaller than the magnetosonic wavelength for this time period, albeit by factors of ~3–5 in the ionosphere and an order of magnitude in the sheath and solar wind.

The ion gyro frequencies are also calculated using the MAVEN observations and are shown in Figure 5e. The light ions, in particular protons, gyrate at frequencies 5–10 times faster than the observed magnetosonic wave frequency. This characteristic means that we expect the protons in particular to follow mostly adiabatic gyromotion around the magnetic field lines, and this is supported by the observations that the proton densities vary in phase with the magnetic field fluctuations (Figures 5a and 5c). In contrast, the heavy ions gyrate ~2–10 times slower than the magnetosonic wave frequency, and we do not expect the heavy ions to follow adiabatic motion. Evidence of this is observed when comparing the variations in heavy ion density with magnetic field fluctuations, and noting that no obvious correlations are present.

4.3.2. The Importance of Doppler Shift

As noted previously, the magnetosonic waves are observed at a frequency of ~0.06 Hz in the spacecraft frame. In order to make meaningful comparisons to other plasma parameters, the importance of Doppler shift effects resulting from spacecraft motion through the ionosphere, and local plasma flows, must be quantified. One can quantify the importance of Doppler shift using Equations 3 through 5:

$$\omega_{obs} = \vec{k} \cdot \overrightarrow{V_{sc}} + \omega_{real} \tag{3}$$

$$\omega_{obs} = kV_{sc}\cos(\theta) + \omega_{real} \tag{4}$$

$$\omega_{real} = \omega_{obs} - \frac{2\pi V_{sc}\cos(\theta)}{\lambda_{MS}} \tag{5}$$

where ω_{obs} is the observed magnetosonic wave period in the spacecraft frame; ω_{real} is the magnetosonic wave period in the plasma frame; $\vec{k}$ is the magnetosonic wave vector, $\overrightarrow{V_{sc}}$ is the spacecraft velocity, and θ is the angle of propagation between $\vec{k}$ and $\overrightarrow{V_{sc}}$. The wave polarization results shown in Figure 2 demonstrate that the WNA of the magnetosonic waves is ~80°, however, without vector electric field measurements (which MAVEN does not make) there is still ambiguity as to the direction of this propagation with respect to the magnetic field and thus spacecraft velocity vector. As such, we have calculated the "worst case" scenario Doppler effect by assuming that the term $\cos(\theta)$ in Equation 5 has its maximum value of ±1. This worst case Doppler shift is shown as a percentage of the observed frequency in Figure 5g. We have made this calculation for the effects of spacecraft motion (V_{sc}) and for local plasma flows. For the latter, we substituted the observed magnitude of ion flow velocities for the V_{sc} term in Equation 5.

Figure 5g shows that within the sheath and solar wind the large values of V_A mean that Doppler shift due to spacecraft motion ("sc") is always negligible. In the dense ionosphere, Doppler shift effects due to spacecraft motion could modify the observed wave frequency by about 20% for the most part. Because the worst case scenario spacecraft Doppler shift effects are relatively small, and the magnetosonic waves appear as monochromatic waves in the wavelet spectrum (Figure 5b), we deem that Doppler shift effects

due to spacecraft motion are negligible here. Were they important, we would expect to see variations in the frequency at which magnetosonic wave power is observed in the wavelet spectrum, as the magnetic field direction changes with respect to the spacecraft. This is not the case, and supports our interpretations.

In contrast to spacecraft motion, the large solar wind proton velocity (relative to V_A, the magnetosonic wave group velocity) in the upstream region means that Doppler shift effects due to local plasma flow are likely important here. This is consistent with studies of waves generated upstream of planetary bow shocks in general, where wave group velocities are typically much slower than solar wind velocities, resulting in the waves being advected back into the shock (Hoppe et al., 1981; Tsurutani et al., 1987). In these cases, the low frequency waves are observed as left-hand polarized in the spacecraft frames (as is observed in Figure 2h), despite being right-hand polarized in the plasma frame.

In the ionosphere, the effects of plasma flow on wave Doppler shift are comparable to those from spacecraft motion and should not produce significant Doppler shift in the spacecraft frame. Protons and O_2^+ are the dominant ion species within the ionosphere for this orbit and their respective flow velocities are shown in Figure 5f. These flow velocities are in the Mars frame, that is, spacecraft potential and spacecraft velocity have been accounted for. The flow velocities are ~2–10 times slower than V_A, and the maximum Doppler shifts are subsequently less than 100%, particularly for O_2^+. Ion flow velocities of these magnitudes ($\lesssim$10 kms$^+$) are not unexpected here because the spacecraft is above the collisional regime of the atmosphere, sampling the nightside and terminator region where large neutral winds and ion flows are expected (Adams et al., 2018; Bougher et al., 2015). In this case, Doppler effects due to local plasma flows are expected to be negligible within the ionosphere.

4.3.3. Steepened Magnetosonic Waves

A zoom in of MAVEN plasma observations during time period 1 (marked in Figure 3) is presented in Figure 6. This zoom in is centered just prior to periapsis covering the period where steepened magnetosonic waves are present, characterized by the sawtooth-like form in the magnetic field amplitude (panel a). As noted previously, variations in proton density occur in phase with the magnetic field fluctuations, while the variations in heavier ion densities do not follow this behavior (panel b). We have divided the time series into seven "wave cycles" (determined by eye) as noted along the top of the figure and by the vertical blue lines. Each wave cycle starts at the leading steepened edge of a wave, spans the peak in magnetic field amplitude, and covers the trailing edge of each wave. Minimum variance analysis that is presented and discussed in Section 4.4 further confirms the identification of these waves as steepened magnetosonic waves.

The energy spectra for protons (panel c) shows evidence of periodic enhancements in temperature (i.e., spread in energy) that occur at the steepened edge of each magnetosonic wave. This is confirmed in panel (f) that shows the proton temperature, derived by fitting a drifting Maxwellian (which accounts for spacecraft ram and spacecraft potential effects) to the STATIC energy spectra observed in panel (c). These periodic enhancements are not obvious for the heavier ions (panels d and e), and these differences are important when interpreting the physical processes governing the postulated wave-particle interactions. In order to confirm the presence of wave-particle interactions and their role in the observed ion heating, we have analyzed the IDFS observed by STATIC in more detail, as a function of time and their phase within each steepened magnetosonic wave cycle.

Figure 7 shows proton IDFS observed by STATIC, and the figure is split into seven panels that correspond to the seven individual wave cycles identified in Figure 6. STATIC measures a full IDFS over 4 s, meaning that STATIC typically observes 4–5 IDFS within any given steepened magnetosonic wave cycle. The individual 4 s IDFS are plotted as the different colored lines in Figure 7, where the colors denote the phase (or time of occurrence) within each wave cycle: in advancing time, colors are black, purple, blue, green, and orange. Black shows the IDFS (or a vertical slice from the energy spectrum in Figure 7c) at the start of each steepened edge, while green and orange show the IDFS at the trailing edge of each wave cycle. Spacecraft potential effects (as measured by STATIC) have been corrected for. The proton IDFS are clearly modulated by the phase of the wave cycle: proton IDFS are extended in energy (i.e., suprathermal tails) at the steepened edge of each cycle (black lines) and "relax" to lower energies throughout the remainder of each wave cycle. This modulation with wave phase strongly supports our earlier interpretations that the protons will follow adiabatic motion within these steepened waves, due to their small gyro radii and high gyro frequency, with respect to the magnetosonic wavelength and wave period.

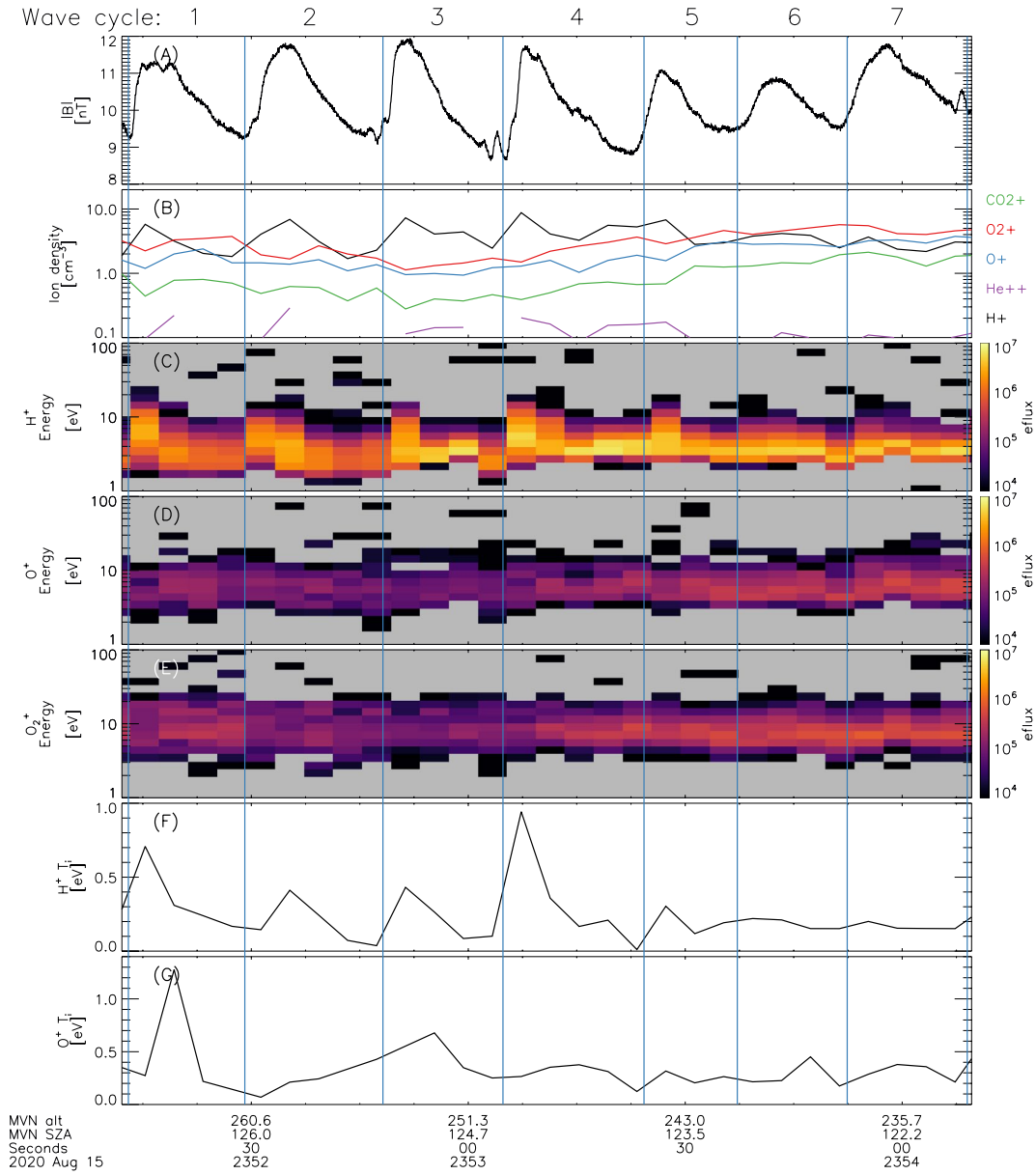

Figure 6. Time series plasma observations of steepened magnetosonic waves close to periapsis. Panels show: (a) magnetic field amplitude; (b) ion densities derived from STATIC observations; (c–e) STATIC energy spectra for protons, O^+ and O_2^+; (f and g): proton and O^+ ion temperatures derived from STATIC observations. The blue vertical lines mark seven individual 'wave cycles', as labeled at the top of the figure.

The format of Figure 8 is the same as Figure 7, except that O^+ IDFS are now displayed. The suprathermal energetic tails are clearly visible, but in contrast to protons, the O^+ IDFS do not appear to be modulated by the phase within each wave cycle. Similar patterns are observed for the O_2^+ IDFS but are not shown here. This behavior also supports our earlier interpretations that the heavier ions likely follow non-adiabatic motion due to their slow gyro periods with respect to the magnetosonic wave period.

4.4. Minimum Variance Analysis of Steepened Magnetosonic Waves

Minimum Variance Analysis (MVA) (Sonnerup & Scheible, 1998) was carried out on the 3D magnetic field observations near periapsis to confirm the presence of steepened magnetosonic waves and the results are shown in Figure 9. The MVA was carried out over the 60 s window covered by panel (a), encompassing

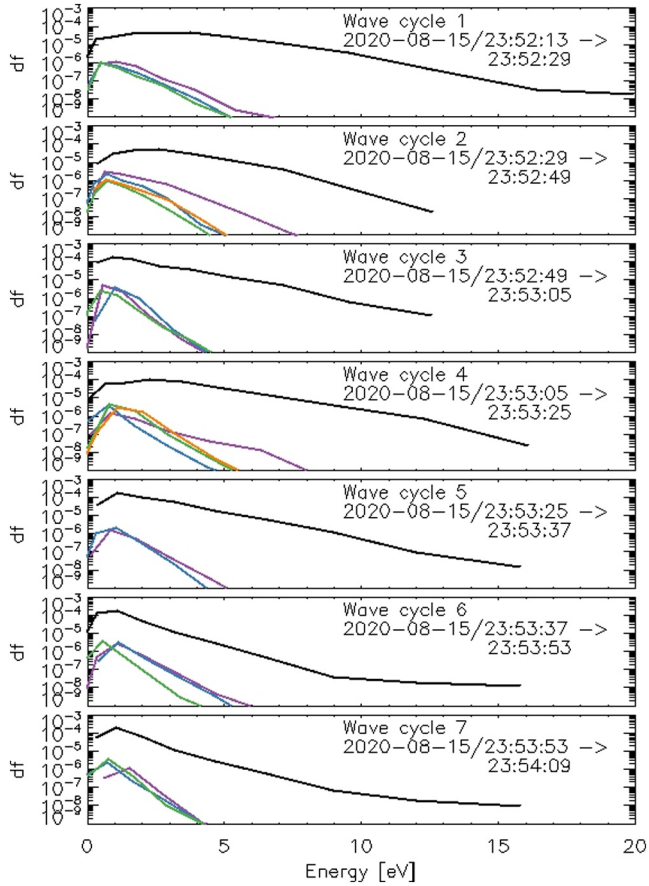

Figure 7. Proton distribution functions measured by STATIC during the seven wave cycles show in Figure 6. Each panel spans a single wave cycle, and individual STATIC 4 s proton distribution functions are plotted within each panel. The line colors mark the phase within each wave cycle that the distribution functions were measured, in advancing time: black, purple, blue, green and orange. df has units of $(km^3\ s^{-3}\ cm^3)^{-1}$. The distributions are corrected for spacecraft potential effects. Spacecraft velocity effects are not accounted for but can be assumed identical for each panel and arise as a ~constant offset in the energy dimension.

three oscillations of the magnetic field. The results and eigenvalue ratios are similar for MVA windows of 30 and 90 s. Panel A shows the magnetic field amplitude of wave cycles 2, 3, and 4 (the wave cycles are marked in Figure 6), where the line color in Figure 9a is a function of time. Periodic, compressive waves are clearly present, that are characterized by a leading steepened edge followed by an extended trailing edge. The hodograms of the various MVA components are shown in panels (b) and (c), where the line color again denotes time and can be compared directly with panel A. The MVA components λ_1, λ_2 and λ_3 denote the minimum, intermediate and maximum variance eigenvalues respectively. Panels (a), (b), and (c) demonstrate that these wave profiles are highly repeatable in nature, with $\frac{\delta B}{|B|}$ on the order of 20%.

Panels (d) and (e) show a zoom in of the single wave cycle enclosed between the gray vertical dashed lines in panel (a). Panel (d) shows the amplitude of the wave, colored based upon the three main segments of the wave: purple marks the region just ahead of the steepened edge (discussed below); gold marks the steepened edge; and brown marks the trailing edge. MVA hodograms of this wave cycle are shown in panels (f) and (g), using the same color scheme. Panel (g) shows that these waves are left hand circularly polarized (in the spacecraft frame), where the leading and steepened edge (purple and gold colors) contribute ~half a phase rotation, and the trailing edge (brown) completes the rotation. These features, in addition to the sawtooth nature of the wave amplitude (panel a), confirm the waves as steepened magnetosonic in nature (Tsurutani et al., 1987, 1989).

Interestingly, the wave hodograms shown in panels (c) and (g) are left-hand polarized, in contrast to the expected right hand polarization for fast magnetosonic waves when observed in the plasma frame. Our Doppler shift analysis (Section 4.3.2) concluded that Doppler shift effects due to spacecraft motion and local plasma flows should be negligible in the ionosphere, and it is currently unclear why left-hand polarization is observed here. One postulation we have is that processes similar to those active in magnetic Pc pulsations may be at play: Pc pulsations can consist of both Alfvénic and compressive-like fluctuations in the magnetic field and theory predicts that the polarization of these waves will switch between right and left handedness as they propagate from the outer to inner magnetosphere (Chen & Hasegawa, 1974). Such behavior has been observed and confirmed by ground and space based measurements (Vellante et al., 2004) at Earth. We have left a detailed investigation of this aspect for future work.

Higher frequency wave trains are also present at the leading edges of the compressive waves (panel a, and purple region panel D). The amplitudes of these wave trains decrease with distance from the steepened edge, matching characteristics reported by Omidi and Winske (1990) and marking them as whistler trains reported by the same authors. These higher frequency waves are thought to arise as a result of the main wave steepening, and are subsequently maintained by currents at the steepened edge. We do not investigate these higher frequency waves further here.

5. Further Discussion and Interpretation

This section presents more detailed discussion of the steepened magnetosonic waves observed around periapsis, and the coincident heated ion populations that we have postulated are subject to wave-particle interactions and energization. In their linear form, magnetosonic waves possess a quasi-sinusoidal-like waveform as observed just after region 3 (~00:10) in Figure 3a. The steepened sawtooth form of these waves,

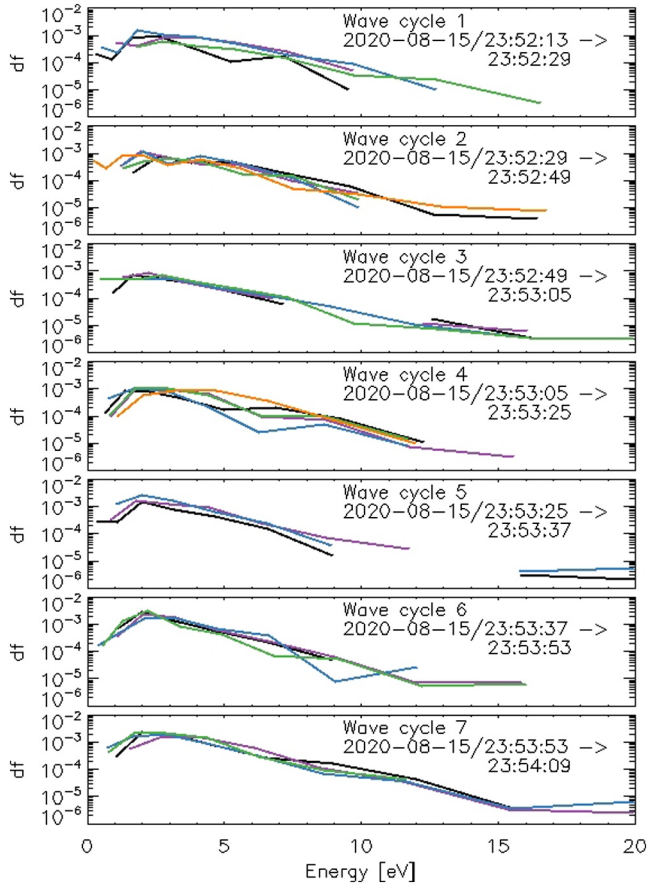

Figure 8. Same format as Figure 7, but for O^+ ion distribution functions measured by STATIC. O_2^+ distributions are similar to O^+, but are not shown.

observed in regions 1 and 2 of Figure 3a, represents a non-linear state of these waves that arises as a natural evolution of the originally quasi-sinusoidal waveforms. Enhancements in the wave phase velocity at the compressional portion of the wave cause the wave to "catch up" with itself, resulting in the steepened waveforms (Matsumoto & Nagai, 1981; Omidi & Winske, 1990; Tsurutani et al., 1987). A variety of theoretical and simulation work has been reported that investigate the processes in which magnetosonic waves (both in the linear and steepened states) can interact with and heat the local plasma in collisionless space environments, and we note those works in the following discussion.

5.1. Heating of Ionospheric Protons by Steepened Magnetosonic Waves

As demonstrated by the plasma parameters shown in Figure 5, the ionospheric protons are magnetized, in that their gyro period is a factor of 5–10 shorter than the magnetosonic wave period, while their gyro radii are at least an order of magnitude smaller than the magnetosonic wavelength. An adiabatic-like response of the protons is thus expected and supported by (a) the in-phase variation of proton density with magnetosonic wave amplitude (Figure 3) and (b) the modulation of the proton temperature and IDFS as a function of phase within the magnetosonic wave cycle (Figures 6f and 7). Using ideal gas theory one can predict the temperature change of the protons due to adiabatic compression driven by the magnetosonic waves, via Equation 6:

$$\frac{T_2}{T_1} = \left(\frac{N_2}{N_1}\right)^{\gamma-1} \tag{6}$$

where T_1 (N_1) and T_2 (N_2) are the proton temperatures (densities) at the trough and peak of a steepened wave edge respectively, and $\gamma = \frac{5}{3}$ for a monatomic gas. Here, the proton gas is effectively compressed by the enhancements in magnetic field strength, as a result of its magnetized nature and associated density enhancements that vary in phase with the magnetic field amplitude. The relationship expressed in Equation 6 has been verified in hybrid simulations of steepened magnetosonic waves in collisionless plasmas (Omidi & Winske, 1990).

The predicted versus observed changes in proton temperature during the steepened magnetosonic waves are calculated using the MAVEN observations shown in Figure 6, and these results are shown in Figure 10. The temperature changes for each of the wave cycles 1–7 are plotted as a cross, and the dashed line shows the 1:1 ratio between the predicted and observed values. The observed values of T_1 and T_2 are taken at the trough and peak of each wave cycle. The predicted temperature change is obtained by using the ratio of the corresponding observed proton densities, as per Equation 6.

Good agreement between the predicted and observed changes in proton temperature is observed for four of the seven wave cycles (2, 5, 6, 7), while the observed temperature change is significantly greater than that predicted for wave cycles 1, 3, and 4. To investigate the discrepancies for wave cycles 1, 3, and 4 further, we wrote computer code that simulates the ion energy spectra observed by STATIC (similar to that used in Hanley et al., 2020), that includes all known instrumental effects as noted in McFadden et al. (2015). Our goal here was to determine if the finite 4 s measurement cadence of STATIC is the cause of the discrepancy between the observed and predicted changes in proton temperature for wave cycles 1, 3, and 4. A full IDF observation by STATIC is comprised of 64 energy × 16 deflector direction measurements (i.e., 1,024 individual measurements) made over four seconds (~3.8 ms per energy-deflector look direction) (McFadden et al., 2015). The instrument sweeps from high to low energies, and at each energy step observes 16 separate deflector directions. Thus, if the ambient plasma changes significantly on timescales comparable to the 4 s

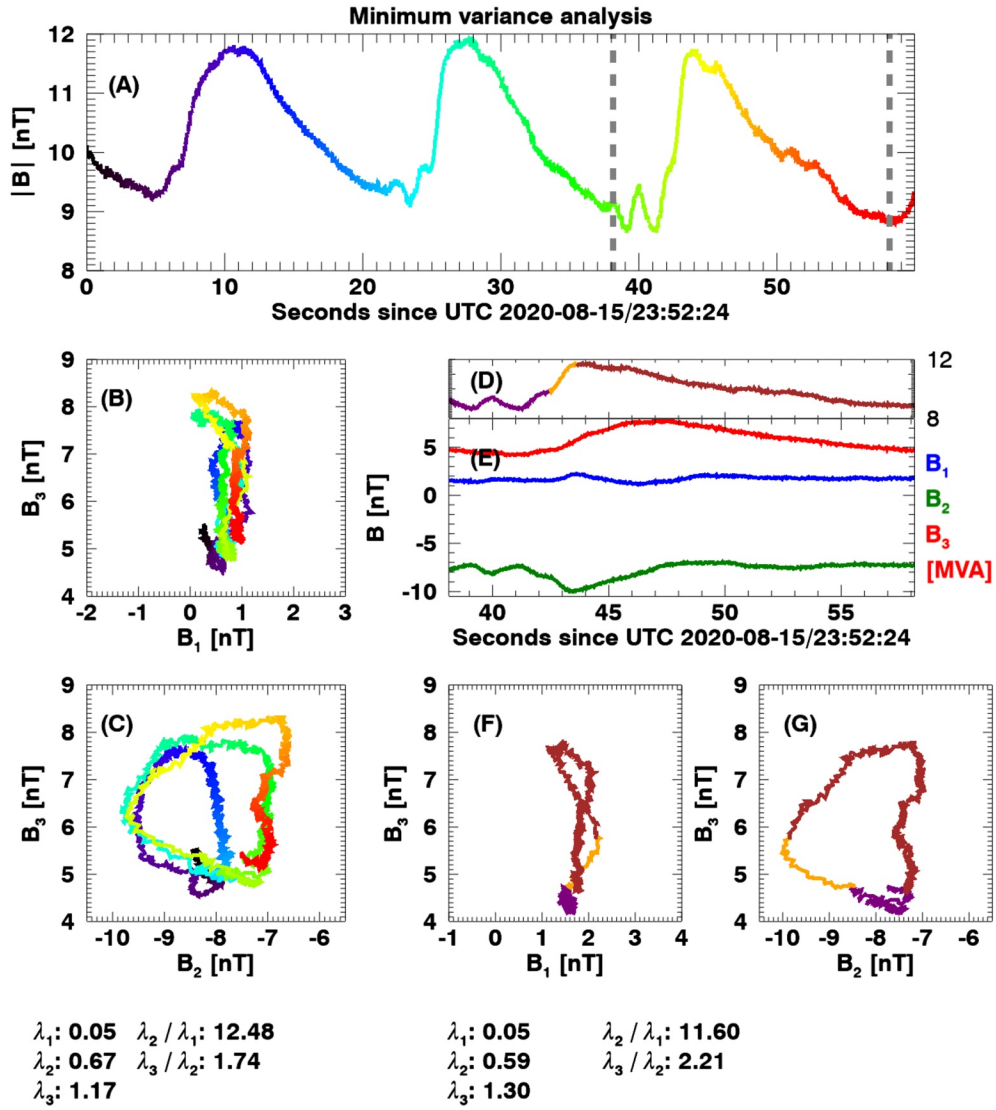

Figure 9. Minimum Variance Analysis of steepened magnetosonic wave cycles 2–4 from Figure 6. Panels shows: (a) magnetic field amplitude, colored as a function of time elapsed during the interval; (b and c): hodograms of the minimum variance components, color coded to match panel (a) (λ_1, λ_2 and λ_3 denote the minimum, intermediate and maximum variance eigenvalues respectively); (d and e) a zoom in on the single steepened wave cycle enclosed by the dashed vertical lines in panel (a) (purple, orange and brown mark higher frequency variations in front of the steepened edge, the steepened edge, and trailing edge, of the wave respectively); (f and g): hodograms of the minimum variance components of the single steepened wave cycle, color coded to match panel (d).

IDF measurement time, these changes are not resolved by the instrument and typically result in artificially enhanced ion temperatures being derived from the observed energy spectra. Although each wave cycle in Figure 6 spans 16–20 s, the steepened edge that compresses the protons can occur over ~4 s and STATIC may thus not fully resolve rapid changes to the IDFS. Our STATIC simulations (more detail provided below but results not shown here) strongly support this theory and explain the discrepancies for wave cycles 1, 3, and 4 in Figure 10 as instrumental in nature, resulting from the finite 4 s measurement cadence of an IDF.

Our virtual STATIC instrument measured a simulated proton population that was assumed to be a drifting Maxwellian, accounting for spacecraft velocity ram and spacecraft potential effects. The density profile of this population was assumed to vary identically in time with the shape of the magnetic field profile shown in Figure 6a (i.e., assuming perfect compression/decompression of the proton population in phase with the magnetosonic wave compressions). The density profile was scaled so that the minimum proton density (at

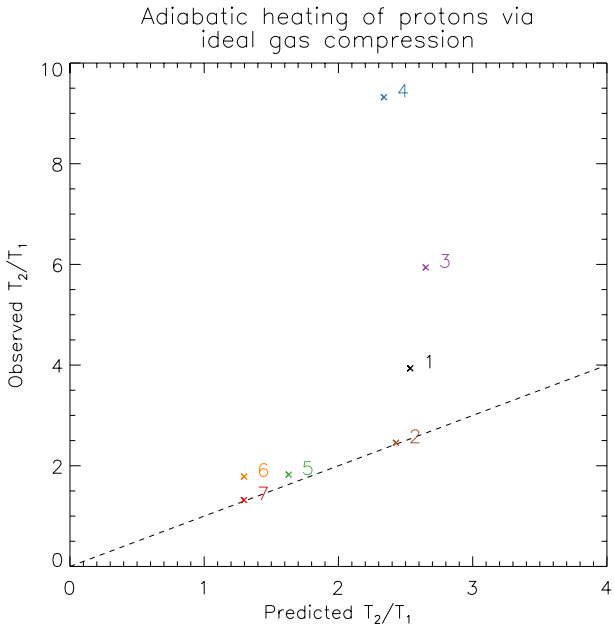

Figure 10. Observed changes in proton temperatures during steepened magnetosonic wave compression, compared to those predicted from adiabatic compression of an ideal proton gas. Wave cycles 1–7 are shown in Figure 6. Predicted temperature changes are calculated using Equation 6.

the magnetic troughs) was 1.5 cm^{-3} while the maximum proton density (at the magnetic peaks) was 7 cm^{-3}. The change in temperature was then calculated using Equation 6 at the same cadence as the magnetic field profile, 32 Hz. We obtained similar results to Figure 10 when using a STATIC measurement cadence of four seconds, in that the temperature changes for 3–4 of the seven simulated wave cycles matched predictions, while the remaining temperature changes were factors of 2–3 higher than predicted. We found that as the integration time required to obtain a simulated STATIC distribution measurement was decreased (i.e., simulated IDFS were obtained more frequently), the temperature changes observed by our simulated instrument asymptotically approached the predicted values, for all seven wave cycles. Significant improvement was gained by halving the STATIC measurement cadence to two seconds, and almost 1:1 behavior was observed for an IDF measurement cadence of one second.

The takeaway from these instrument simulations is that the observed proton heating at periapsis during the steepened magnetosonic waves can be explained by adiabatic compression of the protons via Equation 6, as has been predicted by more detailed hybrid simulations (Omidi & Winske, 1990). Additional sources of proton heating may be present during these wave cycles but are not necessary to explain the observations. Comprehensive hybrid or kinetic simulations of these wave cycles within the Martian environment would be an informative next step to determine the influence of this heating on ionospheric dynamics. The adiabatic nature of this heating means that the protons are not expected to experience a net energy gain during a compressive wave cycle and the impacts of this, particularly on ion escape rates, are not yet clear.

5.2. Heating of Heavy Planetary Ions by Steepened Magnetosonic Waves

The MAVEN observations in Figure 6b show that O^+ and O_2^+ are the primary heavy ion species when the steepened magnetosonic waves are observed close to periapsis. The plasma parameters shown in Figure 5 demonstrate that these heavy ions are unmagnetized: the heavy ion gyro frequencies are roughly an order of magnitude slower than the magnetosonic wave frequency (although, the ion gyro radii are smaller than the magnetosonic wave length by a factor of ~2–3). We subsequently do not expect the heavy ions to respond to the magnetosonic waves in an adiabatic fashion, and this is supported by the facts that (a) the heavy ion densities and temperatures do not vary in phase with the magnetic field fluctuations (Figures 6b and 6g) and (b) the heavy ion IDFS are not modulated with the phase of individual wave cycles (Figure 8).

Fully kinetic simulations of ions and electrons by Lembege et al. (1983); Lembege and Dawson (1984) have shown that for magnetosonic waves characterized by $\omega > \omega_{ci}$ (where ω and ω_{ci} are the wave and ion cyclotron frequencies, respectively) strong ion heating is obtained when the magnetosonic WNA lies in the range ~75°–90°. The ion heating arises from ions becoming trapped in the wave until they are sufficiently heated such that their velocity is greater than the phase velocity of the wave. No resonance conditions are required for this heating to take place. The wave frequency and close-to-perpendicular WNA of the magnetosonic waves observed in Figure 6 satisfy these conditions. The magnetosonic wave phase velocity is approximately equal to the Alfvén speed, which is 10–20 km s^{-1} in the ionosphere (Figure 5f). The thermal velocities of O^+ and O_2^+ ions trapped within such a potential would reach equivalent energies of ~10–30 eV and ~15–60 eV, respectively. The suprathermal tails observed in Figures 4a–4c agree with this expectation, and the MAVEN observations are thus consistent with this wave-trapping mechanism being a candidate for heating the planetary ions. This process is in contrast to the reversible nature of the adiabatic heating of protons that is observed.

5.3. The Significance of Wave Activity and Ion Heating in the Lower Ionosphere

The MAVEN observations demonstrate that planetary protons and heavy ions are heated by the steepened magnetosonic waves at periapsis, which occurs at an altitude of 213 km for this pass. For context, the exobase region at Mars is typically located at an altitude of ~180–200 km (Jakosky et al., 2017), and the observed ion heating at the top of this region may have significant implications for driving ionospheric escape to space. In the simplest case, one can assume that ions may escape when they reach escape velocity in a direction orientated away from the planet; for O^+ and O_2^+ these energies are ~2 and 4 eV respectively at Mars. Heated planetary ions are observed at energies of 10–20 eV in this case study, which are significantly greater than escape energy.

Ion energization that occurs below the exobase region is thought to be somewhat inefficient at driving escape to space, because the ions thermalize over relatively short time scales via collisions with the dense neutral atmosphere (Schunk & Nagy, 2009). The region above the exobase transitions to a collisionless regime, and charged particle motion is governed by electromagnetic forces. Ions energized in this collisionless regime do not thermalize via collisions and are much more likely to escape if they attain escape energy (e.g., Lillis et al., 2017). In addition, ion densities typically remain significant in the ~100 km above the exobase region even on the nightside (e.g., Fowler et al., 2015) meaning that a significant reservoir of ions exists that could drive significant outflow rates if energized to escape energy. For the case study presented here, the peak ionospheric density is a few hundred cm^{-3} (Figure 1d), and this value is 1–2 orders of magnitude smaller than peak ionospheric densities observed on neighboring periapsis passes when large amplitude magnetosonic waves were not present. Possible explanations that explain these apparently reduced peak ion densities include (a) that the presence of the observed magnetosonic waves and ion heating at periapsis has driven ion escape that has significantly eroded the local ionosphere, or (b) that the reduced peak ionospheric density observed in the presented case study is a result of the natural variability of the nightside Martian ionosphere (e.g., Withers et al., 2012; Zhang, Luhmann, & Kliore, 1990), and that these reduced densities are what allow the magnetosonic waves to propagate to such low altitudes. For context, electromagnetic waves induced by the Mars-solar wind interaction are typically observed to propagate down to altitudes of 300 or 400 km at their deepest (Collinson et al., 2018; Fowler et al., 2017, 2018), although these previous studies have focused on dayside events where ionospheric densities can be significantly larger than those on the nightside and thus absorb more wave energy at higher altitudes. A detailed statistical study is required to confirm either of the proposed hypotheses.

Statistical studies of electromagnetic wave power observed in the Martian magnetosphere have shown that the largest wave powers are usually observed at the lowest SZA (i.e., the subsolar point) (Brain et al., 2002; Espley et al., 2004; Fowler et al., 2017; Ruhunusiri et al., 2015) and one may thus intuitively expect the largest ionospheric wave heating events to also be located close to the sub-solar region. As noted above, case studies of ionospheric heating via electromagnetic waves have focused on events observed in the dayside ionosphere and have reported ion energization reaching altitudes down to 300–400 km (Collinson et al., 2018; Fowler et al., 2017, 2018). To our knowledge, the event studied here is the first case study to demonstrate that large amplitude electromagnetic waves generated by the Mars - solar wind interaction are capable of propagating to the nightside ionosphere and driving significant ionospheric heating there. As will be shown in Section 5.4, the compressive magnetosonic waves gain access to the nightside ionosphere, as a result of their propagation perpendicular to the local magnetic field, in combination with the draped nature of the IMF about the Martian obstacle. This perhaps counter-intuitive scenario raises interesting questions about the effectiveness of various wave modes generated at the solar wind interaction region with planetary magnetospheres and their ability to "penetrate" the underlying planetary ionospheres. The case study presented here, and those by Fowler et al. (2018); Collinson et al. (2018), show that magnetosonic waves at Mars are capable of propagating perpendicular to the draped IMF and reaching low altitudes in the Martian ionosphere. Similar draped field conditions exist at most unmagnetized bodies, such as Venus and comets, and these processes may be active at unmagnetized bodies in general. In contrast, at magnetized bodies, Alfvénic-like waves (i.e., waves that travel ~parallel to the magnetic field) can gain access to the ionospheric cusp regions where they can heat planetary ions and drive ion outflow (e.g., André & Yau 1997; Yau & André, 1997). Alfvénic-like waves may thus be of greater importance for the facilitation of energy transfer from the solar wind to the ionospheres of magnetized bodies. Interestingly, the crustal magnetic fields at

Mars can create "miniature" versions of cusp-like regions via magnetic reconnection with the solar wind (Eastwood et al., 2008; Harada et al., 2018), and Alfvénic-like waves may then provide heating at localized regions within the Martian ionosphere. MAVEN's periapsis was far from the strong crustal field regions for the event analyzed here. Additional work is needed to characterize and understand the importance of various electromagnetic wave modes at Mars and their roles in energizing the ionosphere.

As a final note to this discussion, the kinetic theory outlined in Lembege et al. (1983); Lembege and Dawson (1984) also predicts that significant electron heating can occur within these steepened magnetosonic wave events. We have not investigated that aspect here, in part because thermal electron densities and temperatures are not available from the LPW instrument for this periapsis pass. The recent study by Su et al. (2020) demonstrated that Landau damping of ionospheric thermal electrons occurred during a non-steepened magnetosonic wave heating event, and similar heating may be present during the steepened event analyzed in this study. Electron heating can, among other processes, drive ion escape, via ambi-polar electric fields (Ergun et al., 2016), and future work should investigate this aspect in the context of these steepened magnetosonic wave events. Global simulations of the Mars-solar wind interaction are one such tool that can be utilized to understand these effects on a global scale, particularly on ion outflow rates, as these characteristics are difficult to determine using single spacecraft measurements alone.

5.4. Summary of Case Study

The previous sections provided detailed analysis of the MAVEN observations that have allowed us to gain insight into the physical processes active during this steepened magnetosonic wave event. Here, we provide a summary of this study, integrating each of the above results to provide our interpretation of the event as a whole. This summary is depicted in Figure 11, where panels (a–d) provide an overview of the MAVEN data, as previously discussed in Figure 1. Figure 11e shows the time elapsed throughout this segment using color. We have included these overview panels to aid in the interpretation of the MAVEN periapsis pass, which is shown in panel (f).

Referring to Figure 11f, in region 1 upstream of the nominal shock front, the magnetic field is aligned in a quasi-parallel orientation (i.e., magnetic field vector is parallel to the shock normal), supporting our interpretation that the highly disturbed plasma observations here are a result of upstream conditions. We postulate that these conditions give rise to the left hand elliptically polarized ($-1 <$ ellipticity < 0, in the spacecraft frame) 0.06 Hz waves observed here, due to ion instabilities. These waves are associated with pressure pulses that are advected into the magnetopause, driving compressive magnetosonic waves (ellipticity ~0) at the same frequency downstream of the magnetopause. These magnetosonic waves propagate almost perpendicularly across the magnetic field, and the draped nature of the IMF about the planetary obstacle means that these waves propagate toward the planet, as depicted by the orange $\vec{\mathbf{k}}$ vector. The magnetic field whiskers confirm the draped nature of the magnetic field in this region. The cold dense planetary ionosphere is first encountered in region 3 and the observed impacting magnetosonic waves are strongly damped here. This damping is likely because the heavy ions (O^+, O_2^+, and CO_2^+) dominate the ion composition and these ions are expected to respond in a non-adiabatic fashion to the magnetic field fluctuations of the wave, leading to stochastic heating similar to that observed in Fowler et al. (2018). Region 4 is centered around periapsis (marked by the orange star) and is where steepened magnetosonic waves are observed. Our interpretation is that the steepened waves observed here have propagated around the bulge in heavy ionospheric density observed in region 3, showing that localized ionospheric structure can strongly influence the propagation of the magnetosonic waves.

The ability of the draped IMF to "guide" magnetosonic waves into the nightside ionosphere is a particularly interesting result that may have implications for the nightside ionospheric energy budget, its structure, dynamics, and loss of ions to space. To our knowledge, this concept has not received much attention, as one intuitively anticipates the largest amplitude electromagnetic waves (and subsequent ionospheric heating) to occur in the dayside ionosphere. The results presented in this study provide strong evidence that wave heating may also be an important driver of the nightside ionosphere. More work is needed to quantify how often these events occur as a function of local time at Mars, and to determine their efficiency at heating the ionosphere via wave-particle interactions.

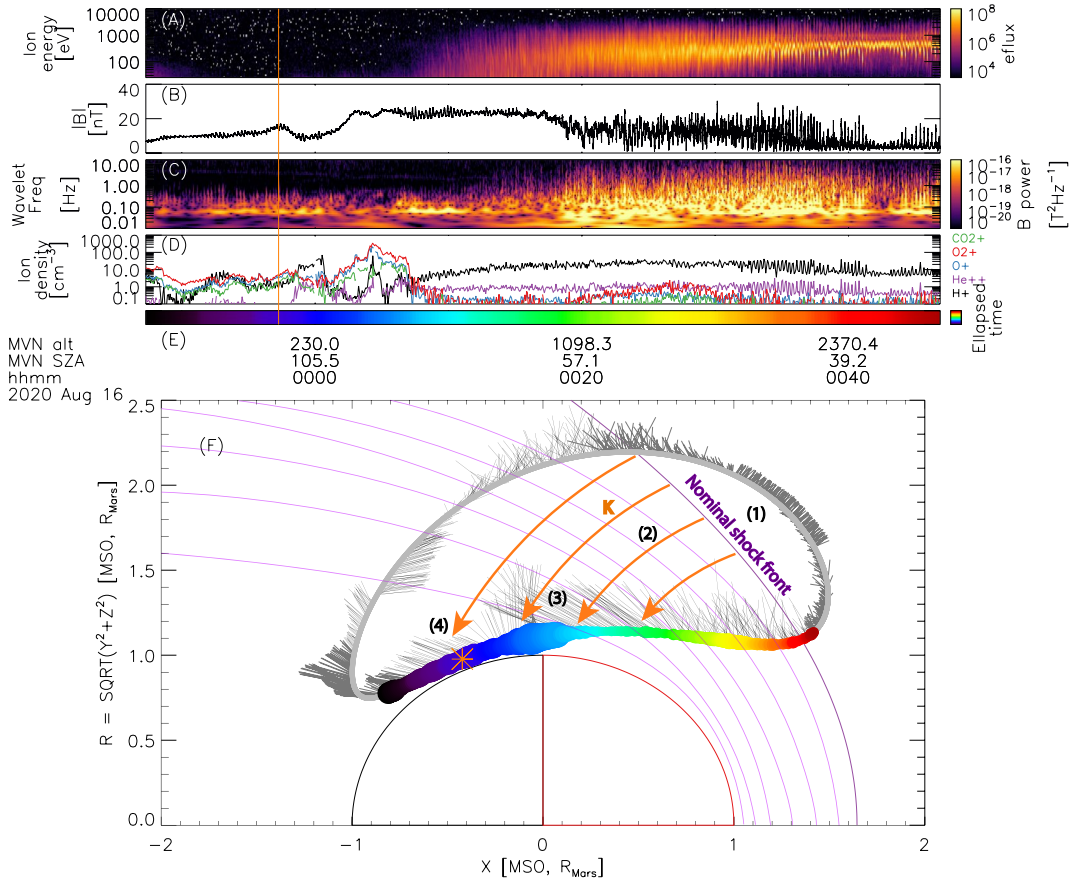

Figure 11. MAVEN observations paired with a cartoon depiction, summarizing the event studied in this paper. Panels show: (a–d) The overview time series plasma observations shown in Figure 1; (e): time elapsed over this interval, coded by color; (f): MAVEN's orbit trajectory in cylindrical Mars Solar Orbital (MSO) coordinates. The gray line is MAVEN's orbit track for the entire ~4.5 h orbit while the colored line segment spans MAVEN's orbit track during the time period shown in panels (a–e). The color of the line can be compared directly to panel E. The thickness of the colored line in panel (f) is proportional to the total heavy ion density ($O^+ + O_2^+ + CO_2^+$) observed by STATIC. The gray whiskers show the magnetic field vector (in cylindrical coordinates) and amplitude (proportional to the length of the whiskers). The thick purple line shows the nominal bow shock location as derived by Vignes et al. (2000); the inner curved purple lines represent draped IMF about the Martian obstacle. The orange lines, labeled **K**, mark the inferred magnetosonic wave propagation vector perpendicular to the draped IMF. The orange star marks the location of periapsis.

5.5. A Note on Magnetic Field Sawtooth Features Previously Observed at Mars

Sawtooth oscillations that are compressional in nature have been previously observed in magnetic field observations within the Martian magnetosphere, made by the Mars Global Surveyor (MGS) (Halekas et al., 2011). The similarities between the MGS and MAVEN magnetic field observations suggest that these phenomena may be related or perhaps the same. The circular orbit (at ~400 km altitude) and lack of ion observations made by MGS meant however that the generation mechanisms and subsequent impact of these sawtooth oscillations on the ionosphere could not be conclusively determined.

Sawtooth-like magnetic structures have also been observed previously at Mars by MAVEN (Halekas et al., 2016), but the characteristics of these "snowplows," as they were termed, leads us to believe that they are not the same phenomenon as the steepened magnetosonic waves observed here. The snowplow structures were associated with the bulk escape of coherent accelerated ionospheric plasma, and appeared as individual large scale structures, as opposed to the wave-train-like nature of the steepened waves observed in this study. Additionally, these snow plows are thought to arise from a process similar to the formation of a diamagnetic cavity, in which differences in ion and electron motion drive ambipolar electric fields that lead to "shielding currents" and the formation of the sawtooth-like magnetic field structure. Although

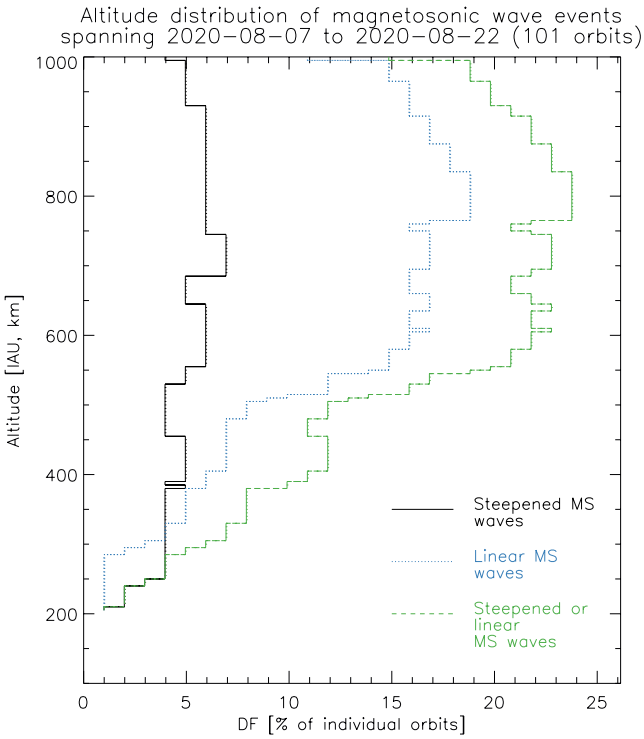

Figure 12. Results of the limited statistical study carried out on 2 weeks (101 orbits) of observations centered on the case study event. DF (distribution function) represents the likelihood of observing magnetosonic waves on any of these 101 orbits, shown as a function of altitude. The colored lines correspond to the three subgroups of magnetosonic wave type, as shown in the figure legend.

the sawtooth-like nature of the magnetic field signature is similar to the steepened waves observed here, the generation mechanisms and physical processes that impact the ionosphere are different.

6. Statistical Study

To place the results of the case study presented here in broader context we have undertaken a limited statistical study focused on MAVEN observations 1 week either side of the case study, spanning dates August 7, 2020 to August 22, 2020 (101 separate orbits). We have determined the occurrence rates of linear and steepened magnetosonic waves observed by the MAVEN magnetometer by eye, at altitudes below 1,000 km. The relatively slow precession of MAVENs orbit means that the local times and SZA sampled by MAVEN during this 2 week period are approximately constant between each periapsis pass. We applied the following criteria to identify wave events by eye, where all five criteria must be satisfied for a candidate event to be recorded. Our selection criteria were applied strictly, meaning that we may have under-counted the number of magnetosonic wave events present.

1. Magnetic field fluctuations must consist of at least five consecutive wave trains.
2. Magnetic field fluctuations are classified as either (a) linear (quasi-sinusoidal) or (b) steepened, in nature.
3. Magnetic field fluctuations must occur at frequencies below 0.1 Hz, to avoid selection of higher frequency waves.
4. Only "clear cut" cases are selected. At times, a variety of wave modes appear present, resulting in "messy" fluctuations in the time series magnetometer observations. These times are not included.
5. The amplitude of the magnetic field fluctuation must be significantly large: $|\delta B| > \pm 1$ nT or $\frac{|\delta B|}{|B|} > 10\%$.

Of the 101 orbits studied, we identified clear examples of steepened magnetosonic waves on 10% of periapsis passes; linear magnetosonic waves on 22% of periapsis passes, and a combination of steepened and/or linear magnetosonic waves on 28% of periapsis passes. These results demonstrate that similar magnetosonic wave events occur somewhat frequently (at least at the terminator and early nightside SZA) and likely play an important role in driving ionospheric dynamics at Mars. The fact that these waves are not observed on all periapsis passes strongly suggests that they occur during specific conditions, the determination of which is left for future work. The case study presented here suggests that pressure pulses upstream of the bow shock may be one such condition required to generate these low frequency compressive waves.

The altitude distributions of the events identified in our statistical study are shown in Figure 12. Wave events are most likely to be observed at and above ~600 km altitude (green dashed line), although this trend is driven mostly by the occurrence rate of linear magnetosonic waves (blue dotted line), which are observed more frequently than their steepened counterparts over all but the lowest altitudes. The upper ionospheric boundary is typically located at similar altitudes, and this trend may indicate the altitude at which these low frequency waves are usually damped by the ionosphere. A more detailed statistical study incorporating the full suite of MAVEN plasma measurements would be able to confirm this supposition.

Steepened magnetosonic waves are observed with roughly constant likelihood above ~250 km, on about 5% of orbits. The lower likelihood of observing steepened magnetosonic waves compared to their linear counterpart suggests that conditions are not usually amenable for the linear waves to evolve into the non-linear steepened regime. Either wave type was observed below altitudes of 400 km on ~8% of orbits, showing that the propagation of these waves into the deep ionosphere is uncommon, but not rare, and the impacts of such events on ionospheric dynamics must be understood.

A detailed statistical study of linear and steepened magnetosonic wave events and their effects on the ionosphere is outside the scope of this report but is however necessary to address the various limitations of the study carried out here. Particular (but not exhaustive) topics that require attention include: the confirmation of the magnetosonic wave generation mechanisms and the conditions under which these mechanisms become active; the occurrence rates of magnetosonic wave events as a function of geographic location, SZA and local time; and a quantification of the influence on global ion escape rates.

7. Conclusions

We have presented in-situ MAVEN plasma observations of low frequency magnetosonic waves that drive significant heating of nightside ionospheric ions via a variety of wave-particle interaction processes. Low frequency, left hand polarized (in the spacecraft frame) waves are observed upstream of the shock, likely driven by instabilities arising in the foreshock region and/or ion pickup. Pressure pulses associated with these waves are advected into the magnetopause by the solar wind flow, and these impacts with the magnetopause generate compressive magnetosonic waves (ellipticity ~0 in the spacecraft frame) at the same frequency downstream of the magnetopause. These magnetosonic waves are originally characterized by quasi-sinusoidal variations in magnetic field amplitude that propagate perpendicular to the local magnetic field. The draped nature of the solar wind IMF results in these waves propagating toward the nightside ionosphere, where they heavily damp upon encountering a localized bulge of cold, dense O^+, and O_2^+ dominated ionospheric plasma, similar to the case study presented by Fowler et al. (2018). Steepened magnetosonic waves, which arise from the evolution of linear magnetosonic waves to a non-linear state, are observed at MAVEN's periapsis at an altitude of 213 km and SZA of 113°. These steepened waves appear to have propagated "around" the enhanced density bulge noted above to reach the nightside ionosphere and are characterized by large amplitude ($\frac{\delta B}{|B|} \sim 20\%$) "sawtooth" fluctuations that are highly repeatable in nature. Minimum Variance Analysis confirms these waves as steepened magnetosonic in nature, including the presence of likely whistler trains at their steepened edges, in accordance with observations at comets and kinetic simulations of these wave modes.

At periapsis, ionospheric protons are observed to respond adiabatically to the steepened magnetosonic waves, leading to heating via adiabatic compression. In contrast, the heavier ions gyrate slowly enough that they respond non-adiabatically to the magnetosonic waves and are heated. Wave-trapping processes are a candidate mechanism to provide this heating, in agreement with previous kinetic simulations of these waves modes. Both the heated proton and heated heavy ion distributions posses suprathermal tails that extend to energies of several 10's of eV, several factors larger than the escape energies (a few eV) of these ions at Mars. This heating may thus drive significant ion escape to space, and global simulations will be required to fully characterize the influence of these waves on ion escape rates.

A limited by-eye statistical study spanning 2 weeks (101 orbits) of data centered on the case study presented here demonstrates that linear and/or steepened magnetosonic waves occur on 28% of these orbits. The magnetosonic waves are most likely to occur at and above ~600 km altitude, with the likelihood of observations decreasing at altitudes below this. Such a trend may arise due to wave damping in the ionosphere, which typically extends to similar altitudes, however, a more detailed study is required to confirm this. Magnetosonic waves were observed below altitudes of 400 km on 8% of orbits, suggesting that although not common, these events occur frequently enough that they may drive significant ion escape over time. Global simulations will again be required to quantify the impacts of these low frequency magnetosonic waves on global ionospheric structure and escape rates in a statistical sense.

Steepened magnetosonic waves have also been observed at comet Giacobini-Zinner and appear to play an important role in the interaction between the comet and solar wind, particularly during times when the comet is active and outgassing. The production of magnetosonic waves may thus play an important role in the interaction between the solar wind and unmagnetized bodies in general. The inferred driving mechanism in this study, the advection of pressure pulses into the magnetopause and resulting generation of magnetosonic waves within the magnetosphere, has been suggested to occur at Mars previously (Collinson et al., 2018) and is analogous to the low frequency magnetic Pc pulsations that occur at Earth. The study of magnetosonic waves and their interaction with charged particles is thus relevant for understanding the

dynamics of, and energy transfer within, the magnetospheres of both unmagnetized and magnetized bodies. Future comparative studies may yield new insights into the wave formation mechanisms and the roles that these waves play within their space plasma environments.

Data Availability Statement

MAVEN data are publicly available at the NASA Planetary Data System (PDS), via https://pds.nasa.gov/.

Acknowledgments
Work at SSL and LASP was supported by NASA funding for the MAVEN project through the Mars Exploration Program under grant number NNH10CC04C.

References

Adams, D., Xu, S., Mitchell, D., Lillis, R., Fillingim, M., Andersson, L., et al. (2018). Using magnetic topology to probe the sources of Mars' nightside ionosphere. *Geophysical Research Letters*, *45*(22), 12–190. https://doi.org/10.1029/2018gl080629

Andersson, L., Ergun, R., Delory, G., Eriksson, A., Westfall, J., Reed, H., et al. (2015). The Langmuir probe and waves (LPW) instrument for MAVEN. *Space Science Reviews*, *195*(1), 173–198. https://doi.org/10.1007/s11214-015-0194-3

André, M., & Yau, A. (1997). Theories and observations of ion energization and outflow in the high latitude magnetosphere. *Space Science Reviews*, *80*(1), 27–48. https://doi.org/10.1007/978-94-009-0045-5_2

Baumjohann, W., & Treumann, R. (2012). *Basic space plasma physics* (Revised Edition). World Scientific Publishing Company.

Bertucci, C., Duru, F., Edberg, N., Fraenz, M., Martinecz, C., Szego, K., & Vaisberg, O. (2011). The induced magnetospheres of Mars, Venus, and Titan. *Space Science Reviews*, *162*(1–4), 113–171. https://doi.org/10.1007/978-1-4614-3290-6_5

Bougher, S., Pawlowski, D., Bell, J., Nelli, S., McDunn, T., Murphy, J., et al. (2015). Mars Global Ionosphere-Thermosphere Model: Solar cycle, seasonal, and diurnal variations of the Mars upper atmosphere. *Journal of Geophysical Research: Planets*, *120*(2), 311–342. https://doi.org/10.1002/2014je004715

Brain, D., Bagenal, F., Acuna, M., Connerney, J., Crider, D., Mazelle, C., et al. (2002). Observations of low-frequency electromagnetic plasma waves upstream from the Martian shock. *Journal of Geophysical Research*, *107*(A6). https://doi.org/10.1029/2000ja000416

Brain, D. A., Mitchell, D. L., & Halekas, J. S. (2006). The magnetic field draping direction at Mars from April 1999 through August 2004. *Icarus*, *182*(2), 464–473. https://doi.org/10.1016/j.icarus.2005.09.023

Chaston, C., Ergun, R., Delory, G., Peria, W., Temerin, M., Cattell, C., et al. (1998). Characteristics of electromagnetic proton cyclotron waves along auroral field lines observed by FAST in regions of upward current. *Geophysical Research Letters*, *25*(12), 2057–2060. https://doi.org/10.1029/98gl00513

Chen, L., & Hasegawa, A. (1974). A theory of long-period magnetic pulsations: 1. Steady state excitation of field line resonance. *Journal of Geophysical Research*, *79*(7), 1024–1032. https://doi.org/10.1029/ja079i007p01024

Chen, R., Cravens, T., & Nagy, A. (1978). The Martian ionosphere in light of the Viking observations. *Journal of Geophysical Research*, *83*(A8), 3871–3876. https://doi.org/10.1029/ja083ia08p03871

Choi, Y., Kim, J., Min, K., Nagy, A., & Oyama, K. (1998). Effect of the magnetic field on the energetics of Mars ionosphere. *Geophysical Research Letters*, *25*(14), 2753–2756. https://doi.org/10.1029/98gl51839

Collinson, G., Wilson, L. B., III, Omidi, N., Sibeck, D., Espley, J., Fowler, C. M., et al. (2018). Solar wind induced waves in the skies of Mars: Ionospheric compression, energization, and escape resulting from the impact of ultralow frequency magnetosonic waves generated upstream of the Martian bow shock. *Journal of Geophysical Research: Space Physics*, *123*(9), 7241–7256. https://doi.org/10.1029/2018ja025414

Connerney, J. E., Espley, J. R., DiBraccio, G. A., Gruesbeck, J., Oliversen, R., Mitchell, D., et al. (2015). First results of the MAVEN magnetic field investigation. *Geophysical Research Letters*, *42*(21), 8819–8827. https://doi.org/10.1002/2015gl065366

Connerney, J. E. P., Espley, J., Lawton, P., Murphy, S., Odom, J., Oliversen, R., & Sheppard, D. (2015). The MAVEN magnetic field investigation. *Space Science Reviews*, *195*, 257–291. https://doi.org/10.1007/s11214-015-0169-4

Cramm, R., Glassmeier, K.-H., Stellmacher, M., & Othmer, C. (1998). Evidence for resonant mode coupling in Saturn's magnetosphere. *Journal of Geophysical Research*, *103*, 11951–11960. https://doi.org/10.1029/98ja00629

Cravens, T., Gombosi, T., Kozyra, J., Nagy, A., Brace, L., & Knudsen, W. (1980). Model calculations of the dayside ionosphere of Venus: Energetics. *Journal of Geophysical Research*, *85*(A13), 7778–7786. https://doi.org/10.1029/ja085ia13p07778

Cravens, T. E. (2004). *Physics of solar system plasmas*. Cambridge University Press.

Cui, J., Galand, M., Zhang, S., Vigren, E., & Zou, H. (2015). The electron thermal structure in the dayside Martian ionosphere implied by the MGS radio occultation data. *Journal of Geophysical Research: Planets*, *120*(2), 278–286. https://doi.org/10.1002/2014je004726

Eastwood, J., Brain, D., Halekas, J., Drake, J., Phan, T., Øieroset, M., et al. (2008). Evidence for collisionless magnetic reconnection at Mars. *Geophysical Research Letters*, *35*(2). https://doi.org/10.1029/2007gl032289

Eastwood, J., Lucek, E., Mazelle, C., Meziane, K., Narita, Y., Pickett, J., & Treumann, R. (2005). The foreshock. *Space Science Reviews*, *118*(1), 41–94. https://doi.org/10.1007/s11214-005-3824-3

Ergun, R., Andersson, L., Fowler, C., Woodson, A., Weber, T., Delory, G., et al. (2016). Enhanced O_2^+ loss at Mars due to an ambipolar electric field from electron heating. *Journal of Geophysical Research: Space Physics*, *121*(5), 4668–4678. https://doi.org/10.1002/2016ja022349

Ergun, R., Andersson, L., Peterson, W., Brain, D., Delory, G., Mitchell, D., et al. (2006). Role of plasma waves in Mars' atmospheric loss. *Geophysical Research Letters*, *33*(14). https://doi.org/10.1029/2006gl025785

Espley, J., Cloutier, P., Brain, D., Crider, D., & Acuña, M. (2004). Observations of low-frequency magnetic oscillations in the Martian magnetosheath, magnetic pileup region, and tail. *Journal of Geophysical Research*, *109*(A7). https://doi.org/10.1029/2003ja010193

Fairfield, D. H. (1971). Average and unusual locations of the Earth's magnetopause and bow shock. *Journal of Geophysical Research*, *76*(28), 6700–6716. https://doi.org/10.1029/ja076i028p06700

Farrugia, C., Freeman, M., Cowley, S., Southwood, D., Lockwood, M., & Etemadi, A. (1989). Pressure-driven magnetopause motions and attendant response on the ground. *Planetary and Space Science*, *37*(5), 589–607. https://doi.org/10.1016/0032-0633(89)90099-8

Fowler, C., Andersson, L., Ergun, R., Harada, Y., Hara, T., Collinson, G., et al. (2018). MAVEN observations of solar wind-driven magnetosonic waves heating the Martian dayside ionosphere. *Journal of Geophysical Research: Space Physics*, *123*(5), 4129–4149. https://doi.org/10.1029/2018ja025208

Fowler, C., Andersson, L., Ergun, R., Morooka, M., Delory, G., Andrews, D. J., et al. (2015). The first in situ electron temperature and density measurements of the Martian nightside ionosphere. *Geophysical Research Letters*, *42*(21), 8854–8861. https://doi.org/10.1002/2015gl065267

Fowler, C. M., Andersson, L., Halekas, J., Espley, J. R., Mazelle, C., Coughlin, E. R., et al. (2017). Electric and magnetic variations in the near-Mars environment. *Journal of Geophysical Research: Space Physics*, *122*(8), 8536–8559. https://doi.org/10.1002/2016JA023411

Glassmeier, K., Volpers, H., & Baumjohann, W. (1984). Ionospheric Joule dissipation as a damping mechanism for high latitude ULF pulsations: Observational evidence. *Planetary and Space Science*, *32*(11), 1463–1466.

Glassmeier, K.-H. (1995). Ultralow-frequency pulsations: Earth and Jupiter compared. *Advances in Space Research*, *16*(4), 209–218. https://doi.org/10.1016/0273-1177(95)00232-4

Glassmeier, K.-H., Klimushkin, D., Othmer, C., & Mager, P. (2004). ULF waves at Mercury: Earth, the giants, and their little brother compared. *Advances in Space Research*, *33*(11), 1875–1883. https://doi.org/10.1016/j.asr.2003.04.047

Halekas, J., Brain, D., & Eastwood, J. (2011). Large-amplitude compressive "sawtooth" magnetic field oscillations in the Martian magnetosphere. *Journal of Geophysical Research*, *116*(A7). https://doi.org/10.1029/2011ja016590

Halekas, J., Brain, D., Luhmann, J., DiBraccio, G., Ruhunusiri, S., Harada, Y., et al. (2017). Flows, fields, and forces in the Mars-solar wind interaction. *Journal of Geophysical Research: Space Physics*, *122*(11), 11–320. https://doi.org/10.1002/2017ja024772

Halekas, J., Brain, D., Ruhunusiri, S., McFadden, J., Mitchell, D., Mazelle, C., et al. (2016). Plasma clouds and snowplows: Bulk plasma escape from Mars observed by MAVEN. *Geophysical Research Letters*, *43*(4), 1426–1434. https://doi.org/10.1002/2016gl067752

Halekas, J., Taylor, E., Dalton, G., Johnson, G., Curtis, D., McFadden, J., et al. (2015). The solar wind ion analyzer for MAVEN. *Space Science Reviews*, *195*(1), 125–151. https://doi.org/10.1007/s11214-013-0029-z

Hanley, K., McFadden, J., Mitchell, D., Fowler, C., Stone, S., Yelle, R., et al. (2020). In situ measurements of thermal ion temperature in the Martian ionosphere. *Journal of Geophysical Research: Space Physics*. https://doi.org/10.1002/essoar.10506971.1. Earth and Space Science open archive - preprint - under review.

Harada, Y., Halekas, J., DiBraccio, G., Xu, S., Espley, J., Mcfadden, J., et al. (2018). Magnetic reconnection on dayside crustal magnetic fields at Mars: MAVEN observations. *Geophysical Research Letters*, *45*(10), 4550–4558. https://doi.org/10.1002/2018gl077281

Hoppe, M., Russell, C., Frank, L., Eastman, T., & Greenstadt, E. (1981). Upstream hydromagnetic waves and their association with backstreaming ion populations: ISEE 1 and 2 observations. *Journal of Geophysical Research*, *86*(A6), 4471–4492. https://doi.org/10.1029/ja086ia06p04471

Jackman, C. M., Thomsen, M. F., & Dougherty, M. K. (2019). Survey of Saturn's magnetopause and bow shock positions over the entire Cassini mission: Boundary statistical properties and exploration of associated upstream conditions. *Journal of Geophysical Research: Space Physics*, *124*(11), 8865–8883. https://doi.org/10.1029/2019ja026628

Jacquinot, J., McVey, B., & Scharer, J. (1977). Mode conversion of the fast magnetosonic wave in a deuterium-hydrogen tokamak plasma. *Physical Review Letters*, *39*(2), 88–91. https://doi.org/10.1103/physrevlett.39.88

Jakosky, B. M., Lin, R. P., Grebowsky, J. M., Luhmann, J. G., Mitchell, D., Beutelschies, G., et al. (2015). The Mars atmosphere and volatile evolution (MAVEN) mission. *Space Science Reviews*, *195*(1), 3–48. https://doi.org/10.1007/s11214-015-0139-x

Jakosky, B. M., Slipski, M., Benna, M., Mahaffy, P., Elrod, M., Yelle, R., et al. (2017). Mars' atmospheric history derived from upper-atmosphere measurements of $^{38}Ar/^{36}Ar$. *Science*, *355*(6332), 1408–1410. https://doi.org/10.1126/science.aai7721

Karney, C., Perkins, F., & Sun, Y.-C. (1979). Alfven resonance effects on magnetosonic modes in large tokamaks. *Physical Review Letters*, *42*(24), 1621–1624. https://doi.org/10.1103/physrevlett.42.1621

Kepko, L., & Spence, H. E. (2003). Observations of discrete, global magnetospheric oscillations directly driven by solar wind density variations. *Journal of Geophysical Research*, *108*(A6). https://doi.org/10.1029/2002ja009676

Lathuillere, C., Glangeaud, F., & Zhao, Z. (1986). Ionospheric ion heating by ULF Pc 5 magnetic pulsations. *Journal of Geophysical Research*, *91*(A2), 1619–1626. https://doi.org/10.1029/ja091ia02p01619

Lembege, B., & Dawson, J. (1984). Plasma heating and acceleration by strong magnetosonic waves propagating obliquely to a magnetostatic field. *Physical Review Letters*, *53*(11), 1053–1056. https://doi.org/10.1103/physrevlett.53.1053

Lembege, B., Ratliff, S., Dawson, J., & Ohsawa, Y. (1983). Ion heating and acceleration by strong magnetosonic waves. *Physical Review Letters*, *51*(4), 264–267. https://doi.org/10.1103/physrevlett.51.264

Lillis, R. J., Deighan, J., Fox, J. L., Bougher, S. W., Lee, Y., Combi, M. R., et al. (2017). Photochemical escape of oxygen from Mars: First results from MAVEN in situ data. *Journal of Geophysical Research: Space Physics*, *122*(3), 3815–3836. https://doi.org/10.1002/2016ja023525

Matsumoto, H., & Barnes, A. (1982). Test particle study of Landau damping of steepening magnetosonic waves. *Journal of Geophysical Research*, *87*(A2), 899–903. https://doi.org/10.1029/ja087ia02p00899

Matsumoto, H., & Nagai, K. (1981). Steepening, soliton, and Landau damping of large-amplitude magnetosonic waves: Particle code computer simulation. *Journal of Geophysical Research*, *86*(A12), 10068–10072. https://doi.org/10.1029/ja086ia12p10068

Matta, M., Galand, M., Moore, L., Mendillo, M., & Withers, P. (2014). Numerical simulations of ion and electron temperatures in the ionosphere of Mars: Multiple ions and diurnal variations. *Icarus*, *227*, 78–88. https://doi.org/10.1016/j.icarus.2013.09.006

Mazelle, C., Winterhalter, D., Sauer, K., Trotignon, J., Acuna, M., Baumgärtel, K., et al. (2004). Bow shock and upstream phenomena at Mars. *Space Science Reviews*, *111*(1), 115–181. https://doi.org/10.1007/978-0-306-48604-3_3

McFadden, J., Kortmann, O., Curtis, D., Dalton, G., Johnson, G., Abiad, R., et al. (2015). MAVEN suprathermal and thermal ion composition (STATIC) instrument. *Space Science Reviews*, *195*(1–4), 199–256. https://doi.org/10.1007/s11214-015-0175-6

Moses, S., Coroniti, F., & Scarf, F. (1988). Expectations for the microphysics of the Mars-solar wind interaction. *Geophysical Research Letters*, *15*(5), 429–432. https://doi.org/10.1029/gl015i005p00429

Omidi, N., & Winske, D. (1990). Steepening of kinetic magnetosonic waves into shocklets: Simulations and consequences for planetary shocks and comets. *Journal of Geophysical Research*, *95*(A3), 2281–2300. https://doi.org/10.1029/ja095ia03p02281

Ostaszewski, K., Glassmeier, K.-H., Goetz, C., Heinisch, P., Henri, P., Ranocha, H., et al. (2020). Steepening of magnetosonic waves in the inner coma of comet 67P/Churyumov-Gerasimenko. *Annales Geophysicae*, *39*, 721–742. https://doi.org/10.5194/angeo–2020–84

Ruhunusiri, S., Halekas, J., Connerney, J., Espley, J., McFadden, J., Larson, D., et al. (2015). Low-frequency waves in the Martian magnetosphere and their response to upstream solar wind driving conditions. *Geophysical Research Letters*, *42*(21), 8917–8924. https://doi.org/10.1002/2015gl064968

Samson, J., & Olson, J. (1980). Some comments on the descriptions of the polarization states of waves. *Geophysical Journal International*, *61*(1), 115–129. https://doi.org/10.1111/j.1365-246x.1980.tb04308.x

Scarf, F., Taylor, W., Russell, C., & Elphic, R. (1980). Pioneer Venus plasma wave observations: The solar wind-Venus interaction. *Journal of Geophysical Research*, *85*(A13), 7599–7612. https://doi.org/10.1029/ja085ia13p07599

Schunk, R., & Nagy, A. (2009). *Ionospheres: Physics, plasma physics, and chemistry*. Cambridge University Press.

Schwartz, S. J., & Burgess, D. (1991). Quasi-parallel shocks: A patchwork of three-dimensional structures. *Geophysical Research Letters*, *18*(3), 373–376. https://doi.org/10.1029/91gl00138

Shan, L., Du, A., Tsurutani, B. T., Yasong, S. G., Lu, Q., Mazelle, C., et al. (2020). In situ observations of the formation of periodic collisionless plasma shocks from fast mode waves. *The Astrophysical Journal Letters*, *888*(2), L17. https://doi.org/10.3847/2041-8213/ab5db3

Shan, L., Ge, Y., & Du, A. (2020). A case study of large-amplitude ULF waves in the Martian foreshock. *Earth and Planetary Physics*, *4*(1), 45–50. https://doi.org/10.26464/epp2020004

Shan, L., Lu, Q., Wu, M., Gao, X., Huang, C., Zhang, T., & Wang, S. (2014). Transmission of large-amplitude ULF waves through a quasi-parallel shock at Venus. *Journal of Geophysical Research: Space Physics*, *119*(1), 237–245. https://doi.org/10.1002/2013ja019396

Shan, L., tsurutani, B. T., Ohsawa, Y., Mazelle, C., Huang, C., Du, A., et al. (2020). Observational evidence for fast mode periodic small-scale shocks: A new type of plasma phenomenon. *The Astrophysical Journal Letters*, *905*(1), L4. https://doi.org/10.3847/2041-8213/abcb02

Shapiro, V., Szegö, K., Ride, S., Nagy, A., & Shevchenko, V. (1995). On the interaction between the shocked solar wind and the planetary ions on the dayside of Venus. *Journal of Geophysical Research*, *100*(A11), 21289–21305. https://doi.org/10.1029/95ja01831

Sibeck, D., Baumjohann, W., & Lopez, R. (1989). Solar wind dynamic pressure variations and transient magnetospheric signatures. *Geophysical Research Letters*, *16*(1), 13–16. https://doi.org/10.1029/gl016i001p00013

Sonnerup, B. U., & Scheible, M. (1998). Minimum and maximum variance analysis. *Analysis methods for multi-spacecraft data*, *1*, 185–220.

Su, Z., Liu, N., Gao, Z., Wang, B., Zheng, H., Wang, Y., & Wang, S. (2020). Rapid landau heating of Martian topside ionospheric electrons by large-amplitude magnetosonic waves. *Geophysical Research Letters*, *47*(20), e2020GL090. https://doi.org/10.1029/2020gl090190

Terasawa, T., & Nambu, M. (1989). Ion heating and acceleration by magnetosonic waves via cyclotron subharmonic resonance. *Geophysical Research Letters*, *16*(5), 357–360. https://doi.org/10.1029/gl016i005p00357

Torrence, C., & Compo, G. P. (1998). A practical guide to wavelet analysis. *Bulletin of the American Meteorological Society*, *79*(1), 61–78. https://doi.org/10.1175/1520-0477(1998)079<0061:apgtwa>2.0.co;2

Tsurutani, B. T., Page, D. E., Smith, E. J., Goldstein, B. E., Brinca, A. L., Thorne, R. M., et al. (1989). Low-frequency plasma waves and ion pitch angle scattering at large distances (¿3.5 × 105 km) from Giacobini-Zinner: Interplanetary magnetic field α dependences. *Journal of Geophysical Research*, *94*(A1), 18–28. https://doi.org/10.1029/ja094ia01p00018

Tsurutani, B. T., Thorne, R. M., Smith, E. J., Gosling, J., & Matsumoto, H. (1987). Steepened magnetosonic waves at comet Giacobini-Zinner. *Journal of Geophysical Research*, *92*(A10), 11074–11082. https://doi.org/10.1029/ja092ia10p11074

Vellante, M., Lühr, H., Zhang, T., Wesztergom, V., Villante, U., De Lauretis, M., et al. (2004). Ground/satellite signatures of field line resonance: A test of theoretical predictions. *Journal of Geophysical Research*, *109*(A6). https://doi.org/10.1029/2004ja010392

Vignes, D., Mazelle, C., Réme, H., Acuña, M., Connerney, J., Lin, R., et al. (2000). The solar wind interaction with Mars: Locations and shapes of the bow shock and the magnetic pile-up boundary from the observations of the MAG/ER Experiment onboard Mars Global Surveyor. *Geophysical Research Letters*, *27*(1), 49–52. https://doi.org/10.1029/1999gl010703

Withers, P., Fillingim, M., Lillis, R., Häusler, B., Hinson, D., Tyler, G., et al. (2012). Observations of the nightside ionosphere of Mars by the Mars Express radio science experiment (MaRS). *Journal of Geophysical Research*, *117*(A12). https://doi.org/10.1029/2012ja018185

Yau, A., & André, M. (1997). Sources of ion outflow in the high latitude ionosphere. *Space Science Reviews*, *80*(1), 1–25. https://doi.org/10.1007/978-94-009-0045-5_1

Zhang, M., Luhmann, J., & Kliore, A. (1990). An observational study of the nightside ionospheres of Mars and Venus with radio occultation methods. *Journal of Geophysical Research*, *95*(A10), 17095–17102. https://doi.org/10.1029/ja095ia10p17095

Zhang, T.-L., Luhmann, J., & Russell, C. (1990). The solar cycle dependence of the location and shape of the Venus bow shock. *Journal of Geophysical Research*, *95*, 14961–14967. https://doi.org/10.1029/ja095ia09p14961